An Interpolation Based Finite Difference Method on Non-uniform Grid for Solving Navier-Stokes Equations

Weijia Chen[1], Jim C. Chen[2], Edmond Y. Lo[3]*
1. ch0003ia@e.ntu.edu.sg; 2. JimChen@ntu.edu.sg; 3. cymlo@ntu.edu.sg.
1, ,2, 3. School of Civil and Environmental Engineering, Nanyang Technological University,
Block N1 Nanyang Avenue, Singapore 639798.

Abstract

This paper presents a Hermite polynomial interpolation based method to construct high-order accuracy finite difference schemes on non-uniform grid. This method can achieve arbitrary order accuracy by expanding the grid stencil and involving higher order derivatives. The paper first constructs combined compact difference schemes, from which compact difference schemes and super-compact difference schemes are shown to be derived by linear operations. Explicit schemes are further shown to be particular cases of this interpolation method. Using the present derivation method, previously reported classical schemes can be constructed on non-uniform grid and a new 5-point combined compact difference scheme is developed in particular. A new 2-piecewise function is also provided for non-uniform grid generation. The first piece of function stabilizes the scheme on Dirichlet boundary by clustering the grid points appropriately and the second piece is to stretch the outer grids according to the simulation domain of interest. This new scheme with non-uniform grid shows excellent stability properties and high spectral resolution as compared with other classical compact and combined compact difference schemes. To further demonstrate the present scheme, simulation of boundary layer transition problems using the three-dimensional incompressible Navier-Stokes equations is performed and good agreement with experimental results is obtained.

Keywords: Compact Difference; Super Compact Difference; Combined Compact Difference; non-uniform grid; polynomial interpolation; Navier-Stokes equations; boundary layer transition.

1. Introduction

For numerical solution of physical problems dominated by multiple length scales, e.g. turbulent flows, stable and accurate numerical methods are needed. Explicit finite difference schemes achieve a certain level of accuracy by extending the stencil to match more terms in Taylor series. However, Lele has shown that if the schemes involve not only the value of the function but also those of its derivatives needed by the simulation, spectral-like resolution can be achieved while keeping a small stencil [1]. These schemes are known as Compact Difference (CD) schemes. The order of accuracy can be even higher if the number and derivative order are increased and such schemes are referred to as Combined Compact Difference (CCD) schemes. Another type of scheme, known as Super Compact Difference (SCD), also demonstrates high order accuracy and they usually involve higher odd or even order of derivatives separately [2].

While different kinds of high order finite difference schemes are widely studied and applied in computations of Navier-Stokes (NS) equations, there is no reported general methodology to construct schemes with arbitrary stencil and accuracy order on non-uniform grids. Chu *et al.* developed a 3-point CCD scheme and later generalized it to non-uniform grids [3, 4], but keeping to the 3-point stencil. Shen *et al.* presented a method for solving unknown coefficients in matching Taylor series to arbitrary high order, but it is not straightforward to extend to non-uniform grids [5]. The non-uniform grid version of a 3-point SCD scheme is derived in [6], but extension of the stencil and accuracy order is not obvious. Shukla *et al.* presented different formulas to derive CD and CCD schemes involving up to second order derivatives on non-uniform grid, but does not develop the method sufficiently to involve arbitrary higher order derivatives [7]. To overcome the limitations of the above methods, this study presents a general method to construct finite difference schemes on non-uniform grid which can involve arbitrary derivative orders, stencils, and thus achieve arbitrary order of accuracy. The derivation method uses the method in [7] as a starting basis but extends the method and incorporates further simplifications.

Another significant problem addressed in this paper is the generation of a non-uniform grid which avoids numerical instability typically seen with high order boundary schemes. Sengupta *et al.* solved this problem by using a pair of low-order explicit schemes to close the 6th-order CCD schemes on uniform grids in [8], while Shukla *et al*. and Hermanns *et al*. introduced a non-uniform grid to address the instability in the boundary region [7, 9]. However, a problem arises when the grid point distribution function required to achieve numerical stability does not satisfy grid stretching imposed by the exterior flow domain of interest, e.g. achieving clustering near a wall boundary and stretching at a far field region using only one function. Therefore, the present study develops a piecewise function having one part near the wall boundary for grid clustering and a second part for grid stretching.

The developed general scheme derivation and non-uniform grid are further used to construct a new 5-point CCD scheme and compared with other classical CD and CCD schemes via stability and spectral analyses. It is further validated by its application in boundary layer transition problems, specifically applied to the wall-normal direction in simulation of the three-dimensional incompressible Navier-Stokes (NS) equations. For such flows, it is well-known that Tollmien–Schlichting (TS) wave interacts resonantly with its initially small amplitude subharmonic wave to generate three-dimensional vortices which break down and finally lead to turbulence. During this transition, high-shear layers usually arise near the wall before flow randomization. The details of this process are discussed in [10-12]. Traditionally, coordinate transform methods for grid clustering in the wall-normal direction can be used to resolve this high-shear region as in [13, 14]. However, Meitz *et al.* showed that the construction of finite difference scheme on non-uniform grids can give more accurate results and the schemes have been applied in boundary layer simulation [15].In this paper, the new CCD scheme is used to simulate subharmonic resonance in boundary layer transition. The total number of grid points used here is significantly reduced compared with reported simulations in [16].

The remainder of the paper is set out as follows. Section 2 presents the general method for deriving finite difference schemes on non-uniform grid. The classical reported high-order schemes are shown to be derived as special cases and a new 5-point 12th order CCD scheme is developed. Section 3 presents the new grid generation function. Sections 4 and 5 analyze the stability properties and spectral resolution of the finite difference schemes on the present non-uniform grid and specifically with the new CCD scheme, demonstrating better performance than the classical schemes. Section 6 applies the new

CCD scheme and non-uniform grid in the wall-normal direction to solve the full 3D incompressible NS equations for the simulation of subharmonic resonance in boundary layer flows.

2. Scheme derivation on non-uniform grid

Scheme construction by interpolation

This section first introduces the derivation of finite difference schemes in the interior domain. The interpolation method described in [7, 17] for deriving finite difference scheme on non-uniform grid is generalized for including higher-order derivatives of arbitrary order and further simplified by matching the order of polynomial interpolation. The approach follows the construction method of Shukla *et al*. in [7], specifically Equations (1) to (9) below which are presented for completeness, and a new simpler procedure is used for the remaining part of derivation. The boundary schemes and other variations on the schemes are derived and discussed in the following sections.

Hermite interpolation for a function $y(x)$ can be written as

$$y(x) = \sum_{d=0}^{D} \sum_{i \in I_n} \rho_{d,i}(x) f^{(d)}(x_i) + \sum_{i \in I_m} r_i(x) f(x_i), \tag{1}$$

where I_n is the point set that defines derivatives $f^{(d)}(x_i)$ up to the D^{th} derivative with function values $f^{(0)}(x_i) = f(x_i)$, and I_m is the point set that defines only the function values $f(x_i)$, which does not overlap with I_n.

The difference schemes can be obtained by differentiating Equation (1) D times for $y^{(k)}(x)$:

$$y^{(k)}(x) = \sum_{d=0}^{D} \sum_{i \in I_n} \rho_{d,i}^{(k)}(x) f^{(d)}(x_i) + \sum_{i \in I_m} r_i^{(k)}(x) f(x_i) \quad \text{for } k = 1, 2, \ldots, D \tag{2}$$

Since

$$y^{(d)}(x_i) = f^{(d)}(x_i) \tag{3}$$

Equation (4) and (5) are thus obtained as

$$\begin{aligned} &\rho_{d,i}^{(0)}(x_j) = \begin{cases} \delta_{ij} & d = 0 \\ 0 & \text{else} \end{cases} && && \forall i \in I_n, \forall j \in I_n \cup I_m \\ &\rho_{d,i}^{(p)}(x_j) = \begin{cases} \delta_{ij} & d = p \\ 0 & \text{else} \end{cases} && p = 1,2 \ldots, D && \forall i \in I_n, \forall j \in I_n \end{aligned} \tag{4}$$

and

$$\begin{aligned} &r_i^{(0)}(x_j) = \delta_{ij} && \forall i \in I_m, \forall j \in I_n \cup I_m \\ &r_i^{(p)}(x_j) = 0 && \forall i \in I_m, \forall j \in I_n \end{aligned} \tag{5}$$

where δ_{ij} is the Kronecker delta.

The following notations are used to derive the expression of unknown polynomials $\rho_{d,i}(x)$ and $r_i(x)$ in Equation (1), following [7]:

$$\prod\nolimits_m (x) := \prod\nolimits_{i \epsilon I_m} (x - x_i), \qquad \prod\nolimits_n (x) := \prod\nolimits_{i \epsilon I_n} (x - x_i), \tag{6}$$

$$l_j^n(x) := \prod_{i=1, i \neq j}^{n} \frac{(x - x_i)}{(x_j - x_i)}, \qquad l_j^m(x) := \prod_{i=1, i \neq j}^{m} \frac{(x - x_i)}{(x_j - x_i)}. \tag{7}$$

Clearly,

$$\prod\nolimits_m (x_i) = 0, i \epsilon I_m, \qquad \prod\nolimits_n (x_i) = 0, i \epsilon I_n, \tag{8}$$

and

$$\begin{aligned} &l_j^n(x_i) = \delta_{ij} \; i \epsilon I_n, && l_j^m(x_i) = \delta_{ij} \; i \epsilon I_m, \\ &l_j^n(x_i) \neq 0 \; i \epsilon I_m, && l_j^m(x_i) \neq 0 \; i \epsilon I_n. \end{aligned} \tag{9}$$

The above decomposition based on the work of [7, 17] are simplified by exploring the polynomial order relationship as follows. The Lagrange polynomial in Equations (7) is of order $n - 1$ with n points. Equation (1), including $\rho_{d,i}(x)$ and $r_i(x)$, defined by $(D + 1)n + m$ grid points should be of order $(D + 1)n + m - 1$. These, together with Equation (4) and (5), lead to the assumption that polynomials $\rho_{d,i}(x)$ and $r_i(x)$ can be decomposed to

$$\rho_{d,i}(x) = \bar{\rho}_{d,i}(x)\frac{\prod_m(x)}{\prod_m(x_i)}\left(l_i^n(x)\right)^{D+1}, \tag{10}$$

and

$$r_i(x) = \left[\frac{\prod_n(x)}{\prod_n(x_i)}\right]^{D+1} l_i^m(x). \tag{11}$$

In the present method, there is no unknown in Equation (11) and the only unknowns in Equation (10) are $\bar{\rho}_{d,i}(x)$. Since $(l_i^n(x))^{D+1}$ is of order (D + 1)(n – 1) and $\frac{\prod_m(x)}{\prod_m(x_i)}$ is of order m, $\bar{\rho}_{d,i}(x)$ should be of order D to make $\rho_{d,i}(x)$ of order (D + 1)n + m – 1, i.e. equal to the order of $y(x)$ in Equation (1). Thus it is only necessary to determine D + 1 polynomials of Dth-order. For each polynomial $\bar{\rho}_{d,i}(x)$, there are (D + 1) unknowns, which can be determined by the corresponding (D + 1) equations in Equations (4). Equation (10) can be differentiated D times to obtain

$$\rho_{d,i}^{(1)}(x) = \bar{\rho}_{d,i}(x)\frac{\prod_m{}'(x)}{\prod_m(x_i)}\left(l_i^n(x)\right)^{D+1} + \frac{\prod_m(x)}{\prod_m(x_i)}\left[\bar{\rho}_{d,i}^{(1)}(x)\left(l_i^n(x)\right)^{D+1} + \bar{\rho}_{d,i}(x)(D+1)\left(l_i^n(x)\right)^{D} l_i^{n\prime}(x)\right] \tag{12a}$$

$$\begin{aligned}\rho_{d,i}^{(2)}(x) = {} & \bar{\rho}_{d,i}(x)\frac{\prod_m{}''(x)}{\prod_m(x_i)}\left(l_i^n(x)\right)^{D+1} + 2\frac{\prod_m{}'(x)}{\prod_m(x_i)}\left[\bar{\rho}_{d,i}^{(1)}(x)\left(l_i^n(x)\right)^{D+1} + \bar{\rho}_{d,i}(x)(D+1)\left(l_i^n(x)\right)^{D} l_i^{n\prime}(x)\right] \\ & + \frac{\prod_m(x)}{\prod_m(x_i)}\Big[\bar{\rho}_{d,i}^{(2)}(x)\left(l_i^n(x)\right)^{D+1} + 2(D+1)\bar{\rho}_{d,i}^{(1)}(x)\left(l_i^n(x)\right)^{D} l_i^{n\prime}(x) \\ & + \bar{\rho}_{d,i}(x)D(D+1)\left(l_i^n(x)\right)^{D-1}\left(l_i^{n\prime}(x)\right)^2 + \bar{\rho}_{d,i}(x)(D+1)\left(l_i^n(x)\right)^{D} l_i^{n\prime\prime}(x)\Big]\end{aligned} \tag{12b}$$

$$\begin{aligned}\rho_{d,i}^{(3)}(x) = {} & \bar{\rho}_{d,i}(x)\frac{\prod_m^{(3)}(x)}{\prod_m(x_i)}\left(l_i^n(x)\right)^{D+1} + 3\frac{\prod_m^{(2)}(x)}{\prod_m(x_i)}\left[\bar{\rho}_{d,i}^{(1)}(x)\left(l_i^n(x)\right)^{D+1} + \bar{\rho}_{d,i}(x)(D+1)\left(l_i^n(x)\right)^{D} l_i^{n\prime}(x)\right] \\ & + \frac{\prod_m{}'(x)}{\prod_m(x_i)}\Big[3\bar{\rho}_{d,i}^{(2)}(x)\left(l_i^n(x)\right)^{D+1} + 6(D+1)\bar{\rho}_{d,i}^{(1)}(x)\left(l_i^n(x)\right)^{D} l_i^{n\prime}(x) \\ & + 3\bar{\rho}_{d,i}(x)D(D+1)\left(l_i^n(x)\right)^{D-1}\left(l_i^{n\prime}(x)\right)^2 + 3\bar{\rho}_{d,i}(x)(D+1)\left(l_i^n(x)\right)^{D} l_i^{n\prime\prime}(x)\Big] \\ & + \frac{\prod_m(x)}{\prod_m(x_i)}\Big[\bar{\rho}_{d,i}^{(3)}(x)\left(l_i^n(x)\right)^{D+1} + 3(D+1)\bar{\rho}_{d,i}^{(2)}\left(l_i^n(x)\right)^{D} l_i^{n\prime}(x) \\ & + 3(D+1)\bar{\rho}_{d,i}^{(1)}(x)\left(D\left(l_i^n(x)\right)^{D-1}\left(l_i^{n\prime}(x)\right)^2 + \left(l_i^n(x)\right)^{D} l_i^{n\prime\prime}(x)\right) \\ & + \bar{\rho}_{d,i}(x)D(D+1)\left((D-1)\left(l_i^n(x)\right)^{D-2}\left(l_i^{n\prime}(x)\right)^3 + 3\left(l_i^n(x)\right)^{D-1} l_i^{n\prime}(x) l_i^{n\prime\prime}(x)\right) \\ & + \bar{\rho}_{d,i}(x)(D+1)\left(l_i^n(x)\right)^{D} l_i^{n\prime\prime\prime}(x)\Big]\end{aligned} \tag{12c}$$

up to $\rho_{d,i}^{(D)}(x)$ as shown in Equation (12) for D = 3

Since $\bar{\rho}_{d,i}(x)$ is a Dth order polynomial, it can be expressed with the unknowns $\bar{\rho}_{d,i}^{(k)}(x_i)$, where k = 0, 1 ,2 , ..., D, as

$$\bar{\rho}_{d,i}(x) = \sum_{k=0}^{D} \frac{1}{k!} \bar{\rho}_{d,i}^{(k)}(x_i)(x - x_i)^k \tag{13}$$

By substituting Equation (13) into Equations (12a) to (12c) and together with Equations (4), one can solve $\bar{\rho}_{d,i}^{(k)}(x_i)$ (d, k = 0, 1, 2, ... , D). To keep to a finite scope, the present study gives the schemes in detail only up to D = 3. The resulting equations of $\bar{\rho}_{d,i}^{(k)}(x_i)$ are given in Table 1.

$d\backslash$	0	1	2	3	...
0	1	$-(D+1)l_i^{n\prime}(x_i)$ $-\frac{\prod_m'(x_i)}{\prod_m(x_i)}$	$-\frac{\prod_m{}''(x_i)}{\prod_m(x_i)} + 2\left[\frac{\prod_m{}'(x_i)}{\prod_m(x_i)}\right]^2$ $+ 2(D+1)\frac{\prod_m'(x_i)}{\prod_m(x_i)} l_i^{n\prime}(x_i)$ $+ (D+1)(D+2)\left[l_i^{n\prime}(x_i)\right]^2$ $- (D+1)l_i^{n\prime\prime}(x_i)$	$-\frac{\prod_m^{(3)}(x_i)}{\prod_m(x_i)} + 3\frac{\prod_m^{(2)}(x_i)}{\prod_m(x_i)}\frac{\prod_m'(x_i)}{\prod_m(x_i)}$ $-\frac{\prod_m{}'(x_i)}{\prod_m(x_i)}\Big[3\bar{\rho}_{0,i}^{(2)}(x_i) + 6(D+1)\bar{\rho}_{0,i}^{(1)}(x_i)l_i^{n\prime}(x)$ $+ 3D(D+1)\left(l_i^{n\prime}(x_i)\right)^2 + 3(D+1)l_i^{n\prime\prime}(x_i)\Big]$ $- 3(D+1)\bar{\rho}_{0,i}^{(2)}(x_i)l_i^{n\prime}(x_i)$ $- 3(D+1)\bar{\rho}_{0,i}^{(1)}(x_i)\left(D\left(l_i^{n\prime}(x_i)\right)^2 + l_i^{n\prime\prime}(x_i)\right)$ $- D(D+1)\left((D-1)\left(l_i^{n\prime}(x_i)\right)^3 + 3l_i^{n\prime}(x_i)l_i^{n\prime\prime}(x_i)\right)$ $- (D+1)l_i^{n\prime\prime\prime}(x_i)$	⋮
1	0	1	$-2(D+1)l_i^{n\prime}(x_i) - 2\frac{\prod_m'(x_i)}{\prod_m(x_i)}$	$-3\frac{\prod_m^{(2)}(x_i)}{\prod_m(x_i)} - 2\frac{\prod_m{}'(x_i)}{\prod_m(x_i)}\left[1.5\bar{\rho}_{1,i}^{(2)}(x_i) + 3(D+1)l_i^{n\prime}(x_i)\right]$ $- 3(D+1)\bar{\rho}_{1,i}^{(2)}(x_i)l_i^{n\prime}(x_i)$ $- 3(D+1)\left(D\left(l_i^{n\prime}(x_i)\right)^2 + l_i^{n\prime\prime}(x_i)\right)$	⋮
2	0	0	1	$-3\frac{\prod_m{}'(x_i)}{\prod_m(x_i)} - 3(D+1)l_i^{n\prime}(x_i)$	⋮
3	0	0	0	1	⋮
⋮	⋮	⋮	⋮	⋮	⋮

Table 1. Coefficients $\boldsymbol{\overline{\rho}_{d,i}^{(k)}(x_i)}$ of the CCD scheme on a non-uniform grid.

The polynomials $r_i^{(k)}(x)$ are similarly obtained by differentiating Equation (11) D times:

$$r_i^{(1)}(x) = (D+1)\left[\frac{\prod_n(x)}{\prod_n(x_i)}\right]^D \left[\frac{\prod_n(x)}{\prod_n(x_i)}\right]' l_i^m(x) + \left[\frac{\prod_n(x)}{\prod_n(x_i)}\right]^{D+1} l_i^{m\prime}(x) \tag{14 a}$$

$$\begin{aligned} r_i^{(2)}(x) = &\left\{D(D+1)\left[\frac{\prod_n(x)}{\prod_n(x_i)}\right]^{D-1} \left[\frac{\prod_n(x)}{\prod_n(x_i)}\right]'^{2} + (D+1)\left[\frac{\prod_n(x)}{\prod_n(x_i)}\right]^{D} \left[\frac{\prod_n(x)}{\prod_n(x_i)}\right]''\right\} l_i^m(x) \\ &+ 2(D+1)\left[\frac{\prod_n(x)}{\prod_n(x_i)}\right]^D \left[\frac{\prod_n(x)}{\prod_n(x_i)}\right]' l_i^{m\prime}(x) + \left[\frac{\prod_n(x)}{\prod_n(x_i)}\right]^{D+1} l_i^{m\prime\prime}(x) \end{aligned} \tag{14 b}$$

$$\begin{aligned} r_i^{(3)}(x) = &\left\{D(D+1)(D-1)\left[\frac{\prod_n(x)}{\prod_n(x_i)}\right]^{D-2} \left[\frac{\prod_n(x)}{\prod_n(x_i)}\right]'^{3} + 3D(D+1)\left[\frac{\prod_n(x)}{\prod_n(x_i)}\right]^{D-1} \left[\frac{\prod_n(x)}{\prod_n(x_i)}\right]^{(1)} \left[\frac{\prod_n(x)}{\prod_n(x_i)}\right]^{(2)}\right. \\ &\left. + (D+1)\left[\frac{\prod_n(x)}{\prod_n(x_i)}\right]^{D} \left[\frac{\prod_n(x)}{\prod_n(x_i)}\right]^{(3)}\right\} l_i^m(x) \\ &+ 3(D+1)\left\{D\left[\frac{\prod_n(x)}{\prod_n(x_i)}\right]^{D-1} \left[\frac{\prod_n(x)}{\prod_n(x_i)}\right]'^{2} + \left[\frac{\prod_n(x)}{\prod_n(x_i)}\right]^{D} \left[\frac{\prod_n(x)}{\prod_n(x_i)}\right]^{(2)}\right\} l_i^{m\prime}(x) \\ &+ 3(D+1)\left[\frac{\prod_n(x)}{\prod_n(x_i)}\right]^{D} \left[\frac{\prod_n(x)}{\prod_n(x_i)}\right]^{(1)} l_i^{m\prime\prime}(x) + \left[\frac{\prod_n(x)}{\prod_n(x_i)}\right]^{D+1} l_i^{m(3)}(x) \end{aligned} \tag{14 c}$$

up to $r_i^{(D)}(x)$ for D = 3.

After the coefficients in Equation (2) are specified, the finite difference schemes are expressed as

$$\begin{aligned} f^{(1)}(x) &= \sum_{d=0}^{D} \sum_{i \in I_n} \rho_{d,i}^{(1)}(x) f^{(d)}(x_i) + \sum_{i \in I_m} r_i^{(1)}(x) f(x_i) \\ f^{(2)}(x) &= \sum_{d=0}^{D} \sum_{i \in I_n} \rho_{d,i}^{(2)}(x) f^{(d)}(x_i) + \sum_{i \in I_m} r_i^{(2)}(x) f(x_i) \\ &\dots \\ f^{(D)}(x) &= \sum_{d=0}^{D} \sum_{i \in I_n} \rho_{d,i}^{(D)}(x) f^{(d)}(x_i) + \sum_{i \in I_m} r_i^{(D)}(x) f(x_i) \end{aligned} \tag{15}$$

For completeness, it is noted the particular case of n = 0 has Equation (1) reducing to the Lagrange interpolation polynomial. Also the explicit finite difference scheme for the D^{th} derivative can be obtained via differentiating D times,

$$f^{(D)}(x) = \sum_{i=1}^{m} r_i^{(D)}(x) f(x_i) \tag{16}$$

Interior scheme

By selecting appropriate point sets I_n and I_m in the above method, arbitrary high-order finite difference schemes can be constructed. Table 2 shows that the present method can be used to construct the classical 3-point centered type schemes on uniform or non-uniform grids, most of which have been widely studied. In the table, the schemes are denoted by: the highest polynomial order, m, n, D, and the step size is denoted by h on uniform grid. Thus, e.g. (6, 2, 1, 2) is a scheme with 6th order polynomial, n = 2, m = 1, and D = 2. As specific cases, the non-uniform grid cases have schemes constructed at x = 0 with point set $I_n = \{-2h, h\}$ and $I_m = \{0\}$ and the step size has been incorporated into the coefficients of the derivatives and function values. CD scheme (4, 2, 1, 1) is the typical CD scheme, given in [1]. Its non-uniform grid version is found in [7]. CCD scheme (6, 2, 1, 2) is the 3-point 6th order CCD scheme, which was first developed in [3] and later extended to non-uniform grid in [4]. CCD scheme (8, 2, 1, 3) involving the third derivative was first reported in [3] and implemented for driven cavity flow simulation in [18]. Its non-uniform grid version can be derived by the present method. In the present study, the formulas in Table 3 are generated first by symbolic operation with Python SymPy library, and then the grid coordinates are substituted with numerical values to give the scheme coefficients, which are next loaded into Fortran for numerical computation.

	Uniform	General non-uniform	Non-uniform with I_n = {-2h, h} and I_m = {0}
CD (4, 2, 1, 1)	$-\frac{3}{4h}f_{i-1}+\frac{3}{4h}f_{i+1}-\frac{1}{4}f_{i-1}^{'}$ $-f_i^{'}-\frac{1}{4}f_{i+1}^{'}=0$	$\frac{2h_2^2}{h_1h_{12}^3}(h_1-h_{12})f_{i-1}+\left(\frac{2}{h_1}+\frac{2}{h_2}\right)f_i+\frac{2h_1^2}{h_2h_{12}^3}(h_2+h_{12})f_{i+1}-\frac{h_2^2}{h_{12}^3}f'_{i-1}-f'_i$ $-\frac{h_1^2}{h_{12}^3}f'_{i+1}=0$	$-\frac{5}{27h}f_{i-1}-\frac{1}{h}f_i+\frac{32}{27h}f_{i+1}$ $-\frac{1}{9}f_{i-1}^{'}-f_i^{'}-\frac{4}{9}f_{i+1}^{'}=0$
CCD (6, 2, 1, 2)	$-\frac{15}{16h^2}f_{i-1}+\frac{15}{16h^2}f_{i+1}$ $-\frac{7}{16h}f_{i-1}^{'}-f_i^{'}$ $-\frac{7}{16h}f_{i+1}^{'}-\frac{1}{16}f_{i-1}^{''}$ $+\frac{1}{16}f_{i+1}^{''}=0$	$\frac{3h_2^2}{h_1h_{12}^5}(-2h_1^2+2h_1h_{12}-h_{12}^2)f_{i-1}+\left(\frac{3}{h_1}+\frac{3}{h_2}\right)f_i$ $+\frac{3h_1^2}{h_2h_{12}^5}(2h_2^2+2h_1h_{12}+h_{12}^2)f_{i+1}+\frac{h_2^3}{h_{12}^4}(3h_1-2h_{12})f^{'}_{i-1}$ $-f'_i+\frac{h_1^3}{h_{12}^4}(3h_2+2h_{12})f'_{i+1}-\frac{h_1h_2^3}{2h_{12}^3}f''_{i-1}-\frac{h_2h_1^3}{2h_{12}^3}f''_{i+1}=0$	$-\frac{29}{162h^2}f_{i-1}-\frac{3}{2h^2}f_i$ $+\frac{155}{81h^2}f_{i+1}-\frac{4}{27h}f_{i-1}^{'}$ $-\frac{1}{h}f_i^{'}-\frac{8}{9h}f_{i+1}^{'}$ $-\frac{1}{27}f_{i-1}^{''}+\frac{4}{27}f_{i+1}^{''}=0$
	$\frac{3}{h^2}f_{i-1}-\frac{6}{h^2}f_i+\frac{3}{h^2}f_{i+1}$ $+\frac{9}{8h}f_{i-1}^{'}-\frac{9}{8h}f_{i+1}^{'}$ $+\frac{1}{8}f_{i-1}^{''}-f_i^{''}$ $+\frac{1}{8}f_{i+1}^{''}=0$	$\frac{h_2^2}{h_1^2h_{12}^5}(-36h_1^3+36h_1^2h_{12}-24h_1^2h_2-18h_{12}^2h_1+18h_1h_2h_{12}-6h_{12}^2h_2)f_{i-1}$ $+\frac{6h_1^2+18h_1h_2+6h_2^2}{h_1^2h_{12}^2}f_i+$ $\frac{6h_1^2}{h_2^2h_{12}^5}(h_{12}^2h_1+3h_1h_2h_{12}+4h_2^2h_1+3h_{12}^2h_2+6h_{12}h_2^2+6h_2^2)f_{i+1}$ $+\frac{6h_2^2}{h_1h_{12}^4}\big(h_1(3h_1-2h_{12})+h_2(2h_1-h_{12})\big)f^{'}_{i-1}$ $+\frac{6h_1^2}{h_2h_{12}^4}\big(h_1(h_{12}+2h_2)+h_2(2h_{12}+3h_2)\big)f^{'}_{i+1}$ $-\frac{h_2^2}{h_{12}^3}(3h_1+2h_2)f''_{i-1}-f''_i-\frac{h_1^2}{h_{12}^3}(2h_1+3h_2)f''_{i+1}=0$	$\frac{131}{162h^2}f_{i-1}-\frac{3}{2h^2}f_i$ $+\frac{56}{81h^2}f_{i+1}+\frac{17}{27h}f_{i-1}^{'}$ $-\frac{8}{27h}f_{i+1}^{'}+\frac{4}{27}f_{i-1}^{''}$ $-f_i^{''}-\frac{4}{27}f_{i+1}^{''}=0$

CCD (8, 2, 1, 3)	$-\frac{35}{32h^3}f_{i-1}+\frac{35}{32h^3}f_{i+1}$ $-\frac{19}{32h^2}f_{i-1}^{'}-\frac{1}{h^2}f_i^{'}$ $-\frac{19}{32h^2}f_{i+1}^{'}-\frac{1}{8h}f_{i-1}^{''}$ $+\frac{1}{8h}f_{i+1}^{''}-\frac{1}{96}f_{i-1}^{'''}$ $-\frac{1}{96}f_{i+1}^{'''}=0$	$\frac{4h_2^4(5h_1^3-5h_1^2h_{12}+3h_1h_{12}^2-h_{12}^3)}{h_1h_{12}^7}f_{i-1}$ $+\frac{4h_1^4(5h_2^3+5h_2^2h_{12}+3h_2h_{12}^2+h_{12}^3)}{h_2h_{12}^7}f_{i+1}$ $+\frac{h_2^4(-10h_1^2+8h_1h_{12}-3h_1h_{12}^2)}{h_{12}^6}f'_{i-1}+\frac{h_1^4(10h_2^2+8h_2h_{12}+3h_{12}^2)}{h_{12}^6}f'_{i+1}$ $+\frac{h_1h_2^4(2h_1-h_{12})}{h_{12}^5}f''_{i-1}-\frac{h_2h_1^4(2h_2+h_{12})}{h_{12}^5}f''_{i+1}-\frac{h_1^2h_2^4}{6h_{12}^4}f'''_{i-1}-\frac{h_1^4h_2^2}{6h_{12}^4}f'''_{i+1}$ $+\left(\frac{4}{h_1}+\frac{4}{h_2}\right)f_i-f'_i=0$	$-\frac{24}{145h^3}f_{i-1}-\frac{2}{h^3}f_i$ $+\frac{314}{145h^3}f_{i+1}-\frac{115}{729h^2}f_{i-1}^{'}$ $-\frac{1}{h^2}f_i^{'}-\frac{976}{729h^2}f_{i+1}^{'}$ $-\frac{14}{243h}f_{i-1}^{''}+\frac{80}{243h}f_{i+1}^{''}$ $-\frac{2}{243}f_{i-1}^{'''}-\frac{8}{243}f_{i+1}^{'''}=0$
	$\frac{4}{h^3}f_{i-1}-\frac{8}{h^3}f_i+\frac{4}{h^3}f_{i+1}$ $+\frac{29}{16h^2}f_{i-1}^{'}-\frac{29}{16h^2}f_{i+1}^{'}$ $+\frac{5}{16h}f_{i-1}^{''}-\frac{1}{h}f_i^{''}$ $+\frac{5h^2}{16h}f_{i+1}^{''}+\frac{1}{48}f_{i-1}^{'''}$ $-\frac{1}{48}f_{i+1}^{'''}=0$	$\frac{h_2^3(160h_1^4-160h_1^3h_{12}+120h_1^3h_2+96h_1^2h_{12}^2-100h_1^2h_{12}h_2-32h_1h_{12}^3+48h_1h_{12}^2}{h_1^2h_{12}^7}$ $-\frac{h_1^3(160h_2^4+160h_2^3h_{12}+96h_{12}^2h_2^2+32h_2h_{12}^2+120h_1h_2^3+100h_2^2h_{12}h_1+48h_1h}{h_2^2h_{12}^7}$ $+\frac{h_2^3(-80h_1^3+64h_1^2h_{12}-60h_1^2h_2-24h_1h_{12}^2+40h_1h_{12}h_2-12h_{12}^2h_2)}{h_1h_{12}^6}f'_{i-1}$ $+\frac{h_1^3(-80h_2^3-64h_2^2h_{12}-24h_{12}^2h_2-60h_1h_2^2-40h_1h_{12}h_2-12h_{12}^2h_1)}{h_2h_{12}^6}f'_{i+1}$ $+\frac{h_2^3\left(8h_1^2(2h_1-h_{12})+h_2\left(-2h_2h_{12}+3h_1(4h_1-h_{12})\right)\right)}{h_1h_{12}^5}f''_{i-1}$ $+\frac{h_1^3\left(8h_2^2(2h_2+h_{12})+h_1\left(2h_2h_{12}+3h_2(4h_2+h_{12})\right)\right)}{h_2h_{12}^5}f''_{i+1}$ $-\frac{h_1h_2^3(4h_1+3h_2)}{3h_{12}^4}f'''_{i-1}-\frac{h_2h_1^3(3h_1+4h_2)}{3h_{12}^4}f'''_{i+1}+\left(\frac{12}{h_2^2}+\frac{32}{h_1h_2}+\frac{12}{h_1^2}\right)f_i-f''_i$ $=0$	$\frac{563}{598h^3}f_{i-1}-\frac{1}{h^3}f_i$ $+\frac{35}{598h^3}f_{i+1}+\frac{626}{729h^2}f_{i-1}^{'}$ $-\frac{704}{729h^2}f_{i+1}^{'}+\frac{73}{243h}f_{i-1}^{''}$ $-\frac{1}{h}f_i^{''}-\frac{112h^2}{243h}f_{i+1}^{''}$ $+\frac{10}{243}f_{i-1}^{'''}-\frac{16}{243}f_{i+1}^{'''}=0$

	$\frac{105}{16h^3}f_{i-1}-\frac{105}{16h^3}f_{i+1}$ $+\frac{105}{16h^2}f_{i-1}^{'}+\frac{105}{16h^2}f_{i+1}^{'}$ $+\frac{15}{8h}f_{i-1}^{''}-\frac{15}{8h}f_{i+1}^{''}$ $+\frac{3}{16}f_{i-1}^{'''}-f_i^{'''}$ $+\frac{3}{16}f_{i-1}^{'''}=0$	$\frac{24h_2^2}{h_1^3h_{12}^7}(30h_1^5-30h_1^4h_{12}+60h_1^4h_2+18h_1^3h_{12}^2-50h_1^3h_{12}h_2+15h_1^3h_2^2-6h_1^2h_{12}^3$ $+24h_1^2h_{12}^2h_2-10h_1^2h_{12}h_2^2-6h_1h_{12}^3h_2+4h_1h_{12}^2h_2^2-h_{12}^3h_2^2)f_{i-1}$ $+\left(\frac{24}{h_2^3}+\frac{144}{h_1h_2^2}+\frac{144}{h_2h_1^2}+\frac{24}{h_1^3}\right)f_i$ $-\frac{24h_1^2}{h_2^3h_{12}^7}(30h_2^5+30h_2^4h_{12}++18h_2^3h_{12}^2+6h_2^2h_{12}^3+60h_2^4h_1$ $+50h_2^3h_{12}h_1+24h_2^2h_{12}^2h_1+6h_1h_{12}^3h_2+15h_1^2h_2^3+10h_1^2h_{12}h_2^2$ $+4h_2h_{12}^2h_1^2+h_{12}^3h_1^2)f_{i+1}$ $+\frac{h_2^2}{h_1^2h_{12}^6}(-360h_1^4+288h_1^3h_{12}-720h_1^3h_2-108h_1^2h_{12}^2$ $+480h_1^2h_{12}h_2-180h_1^2h_2^2-144h_1h_{12}^2h_2+96h_1h_2^2h_{12}$ $-24h_{12}^2h_2^2)f'_{i-1}$ $+\frac{h_1^2}{h_2^2h_{12}^6}(-360h_2^4-288h_2^3h_{12}-108h_2^2h_{12}^2-720h_2^3h_1$ $-480h_2^2h_{12}h_1-144h_1h_{12}^2h_2-180h_1^2h_2^2-96h_2h_1^2h_{12}$ $-24h_{12}^2h_1^2)f'_{i+1}$ $+\frac{12h_2^2}{h_1h_{12}^5}\Big(3h_1^2(2h_1-h_{12})+h_2^2(3h_1-h_{12})$ $+h_2\big(-2h_1h_{12}+3h_1(4h_1-h_{12})\big)\Big)f''_{i-1}$ $-\frac{12h_1^2}{h_2h_{12}^5}\Big(h_1^2(h_{12}+3h_2)+h_1\big(2h_{12}h_2+3h_2(h_{12}+4h_2)\big)$ $+3h_2^2(h_{12}+2h_2)\Big)f''_{i+1}+-\frac{3h_2^2}{h_{12}^4}(2h_1^2+4h_1h_2+h_2^2)f'''_{i-1}$ $-\frac{3h_1^2}{h_{12}^4}(2h_2^2+4h_1h_2+h_1^2)f'''_{i+1}-f'''_i=0$	$-\frac{445}{243h^3}f_{i-1}+\frac{15}{h^3}f_i$ $-\frac{3200}{243h^3}f_{i+1}-\frac{110}{81h^2}f_{i-1}^{'}$ $+\frac{880}{81h^2}f_{i+1}^{'}-\frac{10}{27h}f_{i-1}^{''}$ $-\frac{80}{27h}f_{i+1}^{''}-\frac{1}{27}f_{i-1}^{'''}$ $-f_i^{'''}+\frac{8h^3}{27}f_{i-1}^{'''}=0$

Table 2. 3-point centered type finite difference schemes on uniform, general non-uniform grid, and specific non-uniform grid on I_n = {-2h, h} and I_m = {0}. $h_1=x_0-x_1$, $h_2=x_0-x_2$, and $h_{12}=x_1-x_2$.

A new 5-point centered type CCD schemes is constructed by selecting m = 1 and n = 4. Due to the lengthy mathematical formulas of the general expression, the non-uniform grid is given in Table 3 below with only a specific case, at x = 0, with point sets $I_n = \{-5h, -2h, h, 3h\}$ and $I_m = \{0\}$.

uniform	$i-2$	$i-1$	i	$i+1$	$i+2$
f	$\frac{445}{2592h^2}$	$-\frac{100}{81h^2}$	0	$\frac{100}{81h^2}$	$-\frac{445}{2592h^2}$
f'	$\frac{23}{432h}$	$-\frac{4}{9h}$	$-\frac{1}{h}$	$-\frac{4}{9h}$	$\frac{23}{432h}$
f''	$\frac{1}{216}$	$-\frac{4}{27}$	0	$\frac{4}{27}$	$-\frac{1}{216}$
f	$-\frac{65}{324h^2}$	$\frac{320}{81h^2}$	$-\frac{15}{2h^2}$	$\frac{320}{81h^2}$	$-\frac{65}{324h^2}$
f'	$-\frac{25}{432h}$	$\frac{40}{27h}$	0	$-\frac{40}{27h}$	$\frac{25}{432h}$
f''	$-\frac{1}{216}$	$\frac{8}{27}$	-1	$\frac{8}{27}$	$-\frac{1}{216}$
Non-uniform	$i-2$	$i-1$	i	$i+1$	$i+2$
f	$\frac{1}{967h^2}$	$-\frac{105}{737h^2}$	$-\frac{19}{10h^2}$	$\frac{197}{95h^2}$	$-\frac{1}{31h^2}$
f'	$\frac{27}{32813\,h}$	$-\frac{16}{135\,h}$	$-\frac{1}{h}$	$-\frac{125}{108h}$	$\frac{3}{163h}$
f''	$\frac{5}{27648}$	$-\frac{1}{27}$	0	$\frac{125}{4328}$	$-\frac{1}{341}$
f	$-\frac{2}{453h^2}$	$\frac{131}{172h^2}$	$-\frac{89}{150h^2}$	$-\frac{25}{96h^2}$	$\frac{39}{404h^2}$
f'	$-\frac{1}{287h}$	$\frac{409}{675h}$	0	$\frac{25}{27h}$	$-\frac{42}{745h}$
f''	$-\frac{7}{9216}$	$\frac{8}{45}$	-1	$-\frac{25}{48}$	$\frac{1}{109}$

Table 3. 5-point CCD schemes (12, 4, 1, 2) on uniform, and non-uniform grid with $\boldsymbol{I_n = \{-5h, -2h, h, 3h\}}$ and $\boldsymbol{I_m = \{0\}}$.

Boundary scheme

For schemes involving derivatives with higher order the matrix of spatial discretization will be close to ill-conditioned when boundary schemes with the same order of accuracy as the interior are used [5]. Generally the boundary scheme should lose one order of accuracy to obtain a well-conditioned matrix. Thus in constructing CCD schemes on the boundary, the point set of I_n and I_m should be selected with one or two orders lower accuracy than the interior scheme as shown below.

For the CCD scheme (6, 2, 1, 2) on uniform grid, the work of [3] uses the 4th order schemes given in Table 4 on the boundaries, which can be constructed by selecting m = 2, n = 1 and at the boundary point x = 0 and x = n, respectively. The specific versions of non-uniform grid are also constructed at the point x = 0 with $I_n = \left\{\frac{1}{4}h\right\}$, $I_m = \{0, h\}$ on the left boundary and at the point x = 10 with $I_n = \{9.25h\}$, $I_m = \{9h, 10h\}$ on the right boundary.

	f_0	f_1	f_2	f_0'	f_1'	f_2'	f_0''	f_1''	f_2''
(4, 2, 1, 2)_l uniform	$-\frac{7}{2h^2}$	$\frac{4}{h^2}$	$-\frac{1}{2h^2}$	$-\frac{1}{h}$	$-\frac{2}{h}$	0	0	1	0
	$\frac{9}{h^2}$	$-\frac{12}{h^2}$	$\frac{3}{h^2}$	0	$\frac{6}{h}$	0	−1	−5	0
(4, 2, 1, 2)_l non-uniform	$-\frac{13}{h^2}$	$\frac{352}{27h^2}$	$-\frac{1}{27h^2}$	$-\frac{1}{h}$	$-\frac{20}{9h}$	0	0	$-\frac{1}{6}$	0
	$\frac{120}{h^2}$	$-\frac{1088}{9h^2}$	$\frac{8}{9h^2}$	0	$\frac{88}{3h}$	0	−1	−3	0
	f_{n-2}	f_{n-1}	f_n	f_{n-2}'	f_{n-1}'	f_n'	f_{n-2}''	f_{n-1}''	f_n''
(4, 2, 1, 2)_r uniform	$\frac{1}{2h^2}$	$-\frac{4}{h^2}$	$\frac{7}{2h^2}$	0	$-\frac{2}{h}$	$-\frac{1}{h}$	0	−1	0
	$\frac{3}{h^2}$	$-\frac{12}{h^2}$	$\frac{9}{h^2}$	0	$-\frac{6}{h}$	0	0	−5	−1
(4, 2, 1, 2)_r non-uniform	$\frac{27}{h^2}$	$-\frac{32}{h^2}$	$\frac{5}{h^2}$	0	$\frac{4}{h}$	$-\frac{1}{h}$	0	$-\frac{3}{2}$	0
	$\frac{216}{h^2}$	$-\frac{704}{3h^2}$	$\frac{56}{h^2}$	0	$\frac{40}{h}$	0	0	−11	−1

Table 4. Boundary CD scheme (4, 2, 1, 2) on uniform and non-uniform grid. "_l" denotes the scheme for the left boundary and "_r" for the right boundary.

Scheme variations by linear operation

One limitation of the schemes generated by the above interpolation method is that they include all lower derivatives less than D. In some cases, one may be interested in schemes involving only function values and derivatives with specific derivative order, for example, a CD scheme for the second order derivative. Alternatively, there can be a need to eliminate certain order derivatives or function values at a specific point. Such schemes can be generated using Equations (15) by linear operations of the schemes constructed above. To remove k number of derivatives or function values, k + 1 linearly independent interpolation schemes are arranged to a matrix with the k undesirable derivatives or function values in the first k columns. The matrix is then re-arranged in reduced row echelon form from which the desirable scheme is in the final row of the matrix. The order of the resulting scheme is determined by the lowest order of the interpolation polynomial.

As an example, a 4th order accuracy CD scheme for the second derivatives on uniform grid can be derived from CD scheme (4, 2, 1, 1) and CCD scheme (6, 2, 1, 2) as given in the first three rows of Table 5 (a) below. The 4th row of Table 5 (a) is the derivative on CD scheme (4, 2, 1, 1). Table 5 (b) is the last row of the resulting matrix in reduced row echelon form, obtained by standard Gauss-Jordan elimination with pivoting. This CD scheme is the classical scheme on uniform gird, identical to that derived by Taylor series expansion in [1] and by interpolation in [19]. Extension to non-uniform grid can be achieved by replacing schemes used with their corresponding non-uniform grid versions.

(a)	f'_{i-1}	f'_i	f'_{i+1}	f_{i-1}	f_i	f_{i+1}	f''_{i-1}	f''_i	f''_{i+1}
	$-\frac{7}{16h}$	$-\frac{1}{h}$	$-\frac{7}{16h}$	$-\frac{15}{16h^2}$	0	$\frac{15}{16h^2}$	$-\frac{1}{16h^2}$	0	$\frac{1}{16h^2}$
	$\frac{9}{8h}$	0	$-\frac{9}{8h}$	$\frac{3}{h^2}$	$-\frac{6}{h^2}$	$\frac{3}{h^2}$	$\frac{1}{8}$	-1	$\frac{1}{8}$
	$-\frac{1}{4h}$	$-\frac{1}{h}$	$-\frac{1}{4h}$	$-\frac{3}{4h^2}$	0	$\frac{3}{4h^2}$	0	0	0
	$-\frac{3}{4h}$	0	$-\frac{3}{4h}$	0	0	0	$-\frac{1}{4}$	-1	$-\frac{1}{4}$
(b)	0	0	0	$\frac{1}{h^2}$	$-\frac{2}{h^2}$	$\frac{1}{h^2}$	$-\frac{1}{12}$	$-\frac{5}{6}$	$-\frac{1}{12}$

Table 5. Derivation of CD scheme for the 2nd derivative on uniform grid: (a) the original scheme constructed by interpolation; (b) the last row of matrix in reduced row echelon form.

In addition to recovering CD schemes, the present method is also applicable for deriving SCD schemes that involve odd or even order derivatives separately. The detailed derivation of such scheme is first given in [20]. However, within the present framework, the derivation is much simpler. Here, for example, the two equations of the 6th order SCD scheme for the first derivative are recovered as given in Table 6 (a) and (b) for the uniform grid case. The first equation of the SCD scheme in Table 6 (a) is obtained by combining CCD scheme (8, 2, 1, 3) and the first equation of CCD scheme (6, 2, 1, 2) in Table 2. The second equation in Table 6 (b) is derived by differentiating the CD scheme for the second derivative given in Table 5 (b). The resulting SCD scheme is used in [2].

	f''_{i-1}	f''_i	f''_{i+1}	f'_{i-1}	f'_i	f'_{i+1}	f_{i-1}	f_i	f_{i+1}	f'''_{i-1}	f'''_i	f'''_{i+1}
(a)	0	0	0	0	$\frac{1}{h^2}$	0	$\frac{1}{2h^3}$	0	$-\frac{1}{2h^3}$	$\frac{1}{120}$	$\frac{3}{20}$	$\frac{1}{120}$
(b)	0	0	0	$\frac{1}{h^2}$	$-\frac{2}{h^2}$	$\frac{1}{h^2}$	0	0	0	$-\frac{1}{12}$	$-\frac{5}{6}$	$-\frac{1}{12}$

Table 6. 6th order Supper Compact Difference scheme for the first derivative.

It may also be necessary to construct finite difference schemes with certain derivatives at some particular point. For example, the wall boundary conditions used by [15] requires vanishing of the wall-normal velocity and its first derivative in the wall-normal direction. For these cases, a new scheme can be constructed by removing the second derivative at the particular point from the old scheme. This can be done in analogy with the method given above in deriving Table 6 for uniform grid case.

In summary, the present interpolation based method provides a general and systematic way to construct various classical types of finite difference schemes on non-uniform grid. This includes explicit difference (by Equation (16)), CD, SCD (by Equation (15)) and CCD (by Equation (15)). It can achieve arbitrary high order accuracy and more specialized finite difference scheme can be developed by using different combinations of point sets $I_m$and I_n, and linear operation.

3. Non-Uniform Grid

The finite difference schemes presented in Section 2 can be constructed on an arbitrary non-uniform grid point distribution. However, how to distribute the grid points in high order finite difference schemes is still a difficult problem, because the stability of high order compact difference scheme is a major issue when applied with Dirichlet boundary conditions. Sengupta *et al.* use a pair of 2nd and 3th order explicit schemes to solve the stability problem of CCD (6, 2, 1, 2) scheme on uniform grid [8]. Shukla *et al.* [7, 19] applied a non-uniform grid distribution for high order compact schemes on Dirichlet boundary to solve stability problem. The 12th order CCD scheme for the first derivative is unstable on a uniform grid. Therefore, similar non-uniform grid distribution with [7, 19] is used in the present study to construct stable CCD schemes. Since one usually needs stabilizing clustered grid points on one side and stretched grid points on the other, it is more efficient to use two different equations to implement these two functionalities: one on numerical stability while the other one on stretching grid. Therefore, a piecewise function based on Kosloff *et al.'s* method [21] is proposed as described below.

$$x_i = \begin{cases} x_c\left(1+\dfrac{\operatorname{asin}\left(-\alpha_g\cos\left(\frac{\pi i}{2c}\right)\right)}{\operatorname{asin}(\alpha_g)}\right) & 0 \le i \le c \qquad (17\text{ a}) \\ x_c + (x_c - x_{c-1})\left(\dfrac{\beta_g^{(i-c)}-1}{\beta_g - 1}\right) & c+1 \le i \le n \qquad (17\text{ b}) \end{cases}$$

where α_g and β_g are the grid stretching parameters, c and x_c are the grid index and coordinate of transformation point, respectively, between Equation (17 a) and Equation (17 b). Equation (17 a) originated from [21], which is usually used to stabilize both sides of high-order finite difference boundary schemes as in [7, 9]. Here, it is modified for boundary on one side only. As $\alpha_g \rightarrow 0$, more grid points are clustered to the boundary x_0. The main drawback of Equation (17 a) is that, as $i \rightarrow n$ the distribution is close to a uniform grid which is clearly undesirable for problems that involve a far field region. The proposed modification for grid generation allows for grid clustering up to a certain value $i = c$ while allowing the grid distribution from x_{c+1} to the far field boundary x_n to be stretched.

A simple summation of the geometric sequence, $\{x_i - x_{i-1}\}$, is used for grid stretching in Equation (17 b). This ensures the increment of grid size, $\frac{x_{i+1}-x_i}{x_i-x_{i-1}}$, equals a constant ratio β_g which can be determined by a standard Newton-Raphson method once x_c and x_n are fixed.

The present grid generation function in Equation (17) is compared with other grid generation methods to demonstrate the advantages achieved, including the modified Kosloff's method and Anderson’s method [22]. For this comparison, all the grid generation methods are applied to 80 grid points from x_0 = 0 to x_n = 2.0. Figure 1 is a plot of the grid index i versus grid coordinate x_i for five kinds of grid, including:

1) □ Uniform grid.

2) Δ Modified Kosloff's method (1): Equation (17 a) with α_g = 0.975.

3) ◊ Modified Kosloff's method (2): Equation (17 a) with α_g = 0.6.

4) ○ Present grid generation method in Equation (17) with α_g = 0.975, c = 20, $x_c = x_n/4$.

5) × Anderson’s method [22] which is widely used in boundary layer transition problems

(e.g., [15]) and given by

$$x_i = x_n \frac{(\beta_A + 1) - (\beta_A - 1)\big(((\beta_A + 1)/(1 - \beta_A))^{1-i/n}\big)}{((\beta_A + 1)/(1 - \beta_A))^{1-i/n} + 1} \tag{18}$$

The choice of β_A = 1.1 here is to obtain a similar distribution profile for ready comparison.

As shown in Figure 1, the modified Kosloff's method (1) is close to uniform near i = 80, as discussed above. Modified Kosloff's method (2) stretches grid points near i = 80, but as shown in the small inset, it has a very small minimum grid size at i = 0, resulting a strict stability limitation. The present method from Equation (17) clusters grid points near $i = 0$, but stretches near $i = n$. The small figure inset also shows that the minimum grid space x_1 in the present method is larger than those in the modified Kosloff's methods (1) and (2) with consequent relaxed stability restrictions for time integration. Anderson's method with β_A = 1.1 gives a grid distribution close to that of the present method, but as shown in the following section may lead to potential numerical instability when used with CCD schemes.

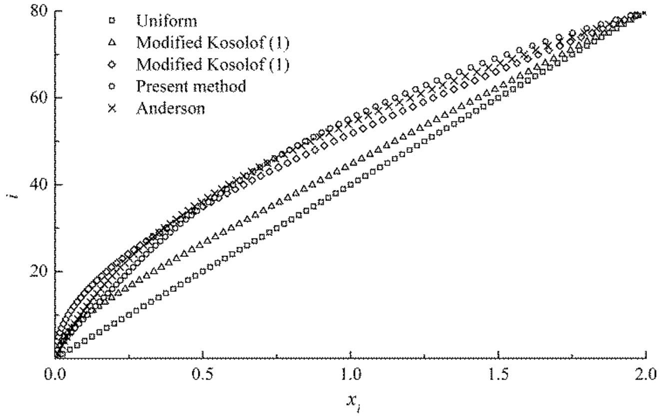

Figure 1. Grid distribution with *n* = 80. The modified Kosloff' method (1): α_g = 0.975; the modified Kosloff's method (2): α_g = 0.6; the present method: α_g = 0.975, *c* = 20, x_c = 0.25; Anderson's method: β_A = 1.1. The vertical axis indicates the grid index *i*, while the horizontal axis shows the grid point coordinates x_i.

4. Stability analysis

An important concern for a numerical method is its stability. This section analyzes the stability problem when the finite difference schemes derived in Section 2 are constructed on the grids given in Section 3. The method used to analyze the spatial stability of scheme is first described and the stability of first- and second-order derivative are then analyzed.

Stability analysis of spatial schemes

The numerical stability of finite difference schemes with boundary closures can be analyzed through the eigenvalue spectrum of the discretization matrix, as described in [23]. The approach is demonstrated in a one-dimensional linear PDE written as:

$$\frac{\partial u}{\partial t} = \mathcal{L}(u) \tag{19}$$

where $\mathcal{L}$ represents a linear combination of the first and second derivatives.

$\mathcal{L}$ can be discretized by the finite difference schemes on uniform or non-uniform grid distributions with appropriate boundary conditions applied. The analysis procedure of CCD schemes with the first and second derivatives is presented as an example and analysis of CD or CCD schemes with higher derivatives can be performed similarly. The CCD schemes can be implemented in the matrix form as

$$\begin{aligned} [A_1]\{u'\} + [B_1]\{u''\} + [C_1]\{u\} + \{b_1\} = 0 \\ [A_2]\{u'\} + [B_2]\{u''\} + [C_2]\{u\} + \{b_2\} = 0 \end{aligned} \tag{20}$$

where $[A_1]$, $[B_1]$, $[C_1]$, $[A_2]$, $[B_2]$, and $[C_2]$ are the coefficient matrices of the CCD scheme, and $\{b_1\}$ and $\{b_2\}$ represent the vectors for boundary values.

After manipulation, the first and second derivatives can be expressed as,

$$\{u'\} = -[A_1 - B_1B_2^{-1}A_2]^{-1}[C_1 - B_1B_2^{-1}C_2]\{u\} - [A_1 - B_1B_2^{-1}A_2]^{-1}\{b_1 - B_1B_2^{-1}b_2\} \tag{21 a}$$

$$\{u''\} = -[B_2 - A_2A_1^{-1}B_1]^{-1}[C_2 - A_2A_1^{-1}C_1]\{u\} - [B_2 - A_2A_1^{-1}B_1]^{-1}\{b_2 - A_2A_1^{-1}b_1\} \tag{21 b}$$

By substituting Equation (21) into Equation (19), one obtains

$$\frac{\partial u}{\partial t} = [\mathcal{L}]\{u\} + \{\mathcal{B}\} \tag{22}$$

where $[\mathcal{L}]$ is a linear combination of $-[A_1 - B_1B_2^{-1}A_2]^{-1}[C_1 - B_1B_2^{-1}C_2]$ and $-[B_2 - A_2A_1^{-1}B_1]^{-1}[C_2 - A_2A_1^{-1}C_1]$, and $\{\mathcal{B}\}$ is a linear combination of

$-[A_1 - B_1 B_2^{-1} A_2]^{-1}\{b_1 - B_1 B_2^{-1} b_2\}$ and $-[B_2 - A_2 A_1^{-1} B_1]^{-1}\{b_2 - A_2 A_1^{-1} b_1\}$. A necessary but not always sufficient condition for spatial stability is that

$$Re(\mathcal{L}_j) \leq 0 \qquad \text{for all } j \tag{23}$$

where $\mathcal{L}_j$ are the eigenvalues of matrix $[\mathcal{L}]$ and $Re(\quad)$ denotes the real part [23].

First order derivative with boundary closure

The following typical one-dimensional convection equation is used to investigate the spatial stability of finite difference schemes for the first derivative, as in the analyses in [7, 9].

$$\frac{\partial u}{\partial t} + \frac{\partial u}{\partial x} = 0 \tag{24}$$

The Dirichlet boundary condition over the computational domain $[0,2]$ is applied:

$$u(0,t) = \sin(\pi t) \tag{25}$$

This test case has a time periodic solution given as

$$u(x,t) = \sin\big(\pi k (t - x)\big) \tag{26}$$

where k = 1 in this section.

Figure 2 shows the eigenvalue plot of the different finite difference schemes developed. To limit the scope of the comparison, Figure 2 is for the new 5-point CCD schemes given in Table 3 with the classical 3-point CD and CCD schemes in Table 2. The latter have been reported in [1, 4, 7, 18]. For completeness, the 5-point 8th order CD scheme, which has been studied in [7, 19], is also added for comparison. The boundary schemes are constructed with one or two orders lower than the interior scheme and the Dirichlet boundary point is defined in point set I_m of Equations (10) and (11). The numerical stability of the schemes can be numerically shown to be independent of the number of grids, so only the cases with n = 80 are shown here. Figure 2 (a) to (e) show that the CD and CCD schemes constructed on the non-uniform grid given by Equation (17) only have non-positive real parts in their eigenvalues, i.e. numerically stable. Figure 2 (f) shows the results for the CCD scheme (12, 4, 1, 2) constructed on Anderson's grid generation method of Equation (18). Real eigenvalues, indicating instability, are seen even though Anderson's method gives a similar grid distribution as the present method (see Figure 1).

To further demonstrate the instability problem, Equation (24) is solved using a 4th order Runge-Kutta scheme for time integration as given in [24]. The numerical solutions with Δt selected to be small of 0.001 is shown in Figure 3 to further verify the stability properties. At time t = 0.1, numerical oscillation is seen near the Dirichlet boundary at x = 0 when using Anderson's method and the solution becomes completely unstable after a few further time steps. In contrast, with the present grid generation method, the numerical solution exhibit a good match to the exact solution as shown up to t = 10.21 (more than 5 periods). Since the periodicity of the solution from boundary condition in Equation (26), a time level t = 10.21 with similar solution at t = 0.1 is presented.

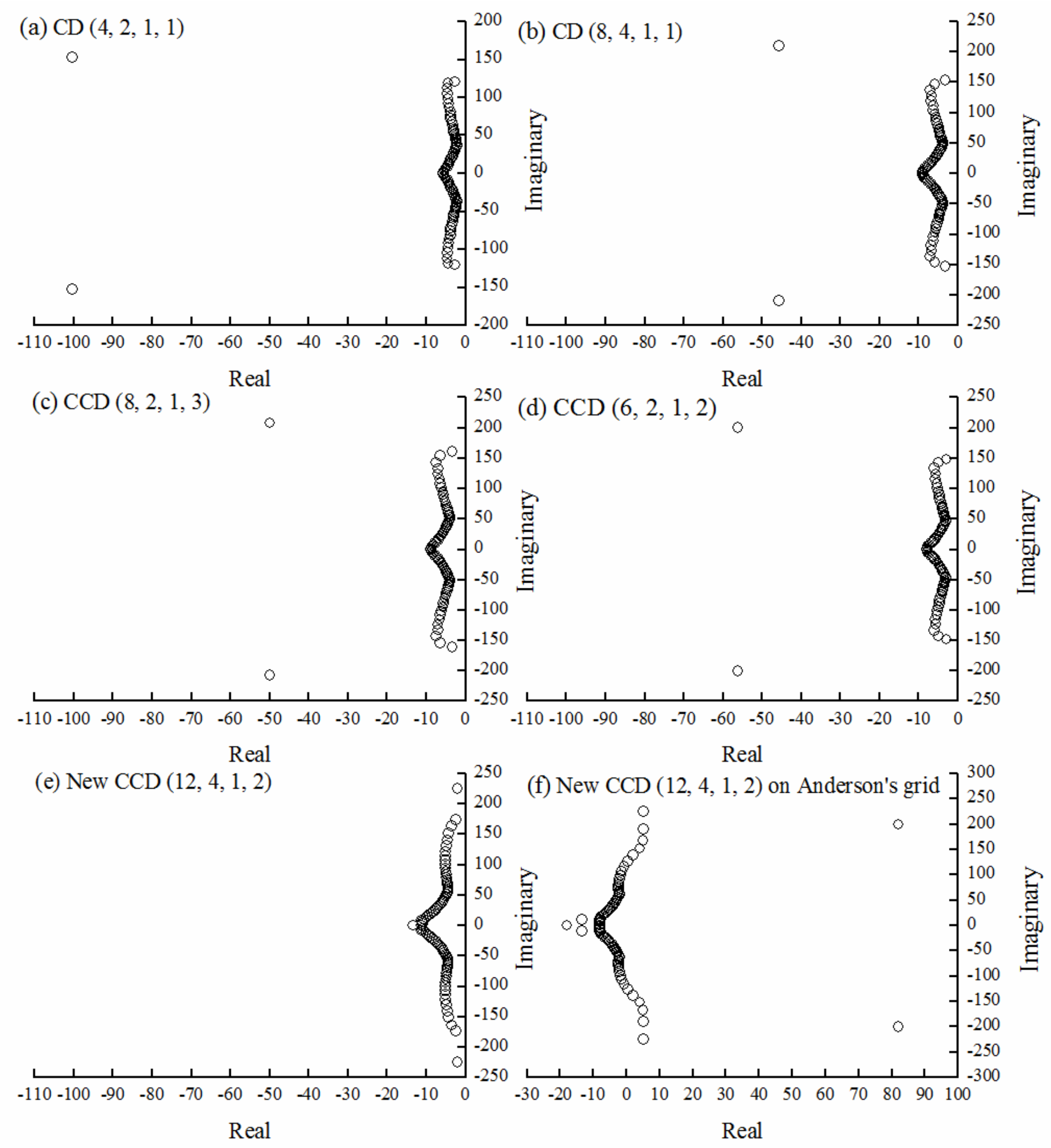

Figure 2. Eigenvalue spectrum for convection operator showing the real and imaginary parts of the eigenvalues for the CD and CCD schemes constructed using the grid generation method of Equation (17): (a) CD (4, 2, 1, 1); (b) CD (8, 4, 1, 1); (c) CCD (8, 2, 1, 3); (d) CCD (6, 2, 1, 2) and (e) New CCD (12, 4, 1, 2). (f) is for new CCD (12, 4, 1, 2) but using Anderson's grid generation method in Equation (18).

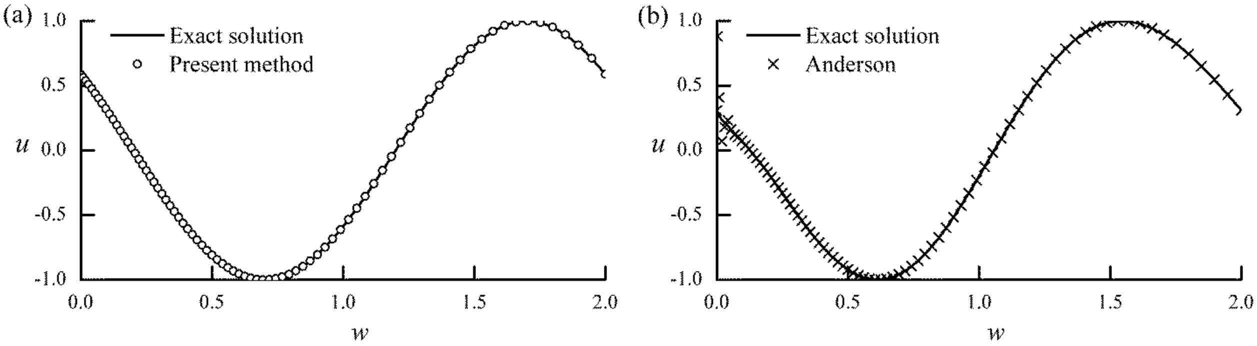

Figure 3. Numerical solutions of the convection equation. (a) Present method at t = 10.21. (b) Anderson's method at t = 0.1 showing instability developing at x = 0.

Second order derivative with boundary closure

The prototypical one-dimensional convection-diffusion equation below is used to investigate the scheme stability under combined first and second derivatives (e.g. [9]).

$$\frac{\partial u}{\partial t}+\frac{\partial u}{\partial x}=\frac{\partial^2 u}{\partial x^2} \tag{27}$$

The following Dirichlet and far field boundary condition over the computational domain [0,60] are applied:

$$u(0,t)=0 \tag{28}$$

and

$$u(x,t)=\frac{\partial u}{\partial x}=\frac{\partial^2 u}{\partial x^2}=0 \qquad \text{at } x=x_n \tag{29}$$

These boundary conditions presume that diffusion effects are sufficiently significant for the solution to vanish at the far field boundary, resulting in Equation (29). The initial conditions are in the form of a wave packet:

$$u(x,0)=\exp(-0.05(x-30)^2+0.1)\sin(1.1x) \tag{30}$$

The eigenvalue spectrum of the new 5-point CCD scheme and the other classical schemes, which have been reported in [1, 4, 7, 18], are shown in Figure 4. There are no positive real parts in the eigenvalues seen for all of these discretizations. The eigenvalue spectrum have spread towards more negative values as compared to that shown in Figure 2 for the schemes constructed on the non-uniform grid of Equation (17) as shown in Figure 4 (a) to (e). This is due to the introduction of operator $\frac{\partial^2}{\partial x^2}$. Figure 4 (f) shows the spectrum of the new CCD scheme (12, 4, 1, 2) on the modified Kosloff's grid (2). The extreme value of this spectrum is much bigger than the same scheme on the present grid shown in Figure 4 (e). Therefore, the temporal step size should be less strict in present grid compared with modified Kosloff's method (2). Since the largest eigenvalue of $\mathcal{L}_j$ exclusively comes from the operator $\frac{\partial^2}{\partial x^2}$, a 2$^{\text{nd}}$ order Strong Stability Preserving Runge-Kutta (SSP-RK) scheme first developed in [31] and following [25] should be used to integrate the term $\frac{\partial^2}{\partial x^2}$, while the 4th order Runge-Kutta scheme is used to integrate $\frac{\partial}{\partial x}$ to preserve low-dispersion and low-dissipation following [30] and extensions in [24]. The details of such a scheme is discussed in the PhD thesis of [26] and outlined in Appendix A.

A numerical solution to Equation (27) integrated by the SSP-RK scheme can be used to demonstrate the stability analysis. Figure 5 plots the numerical solutions of Equation (27) with CCD scheme (12, 4, 1, 2) constructed on the present grid and the Modified Kosloff grid (2). With the present method, a maximum Δt = 0.035 (calculated by Equation (A.5) in Appendix A) can be used for integration to a longer time (e.g. Figure 5 (a) plotted at t = 0.42 and t = 1.75) without instability and having the solution be smoothly damped away. For the modified Kosloff's method (2), Δt is selected to be 0.0015, which is slightly larger than the maximum temporal step restriction evaluated by Equation (A.5). As a result the solution starts to oscillate near the wall boundary at t = 0.078. Such strict stability restriction makes it impractical to apply explicit temporal integration with the modified Kosloff's method (2).

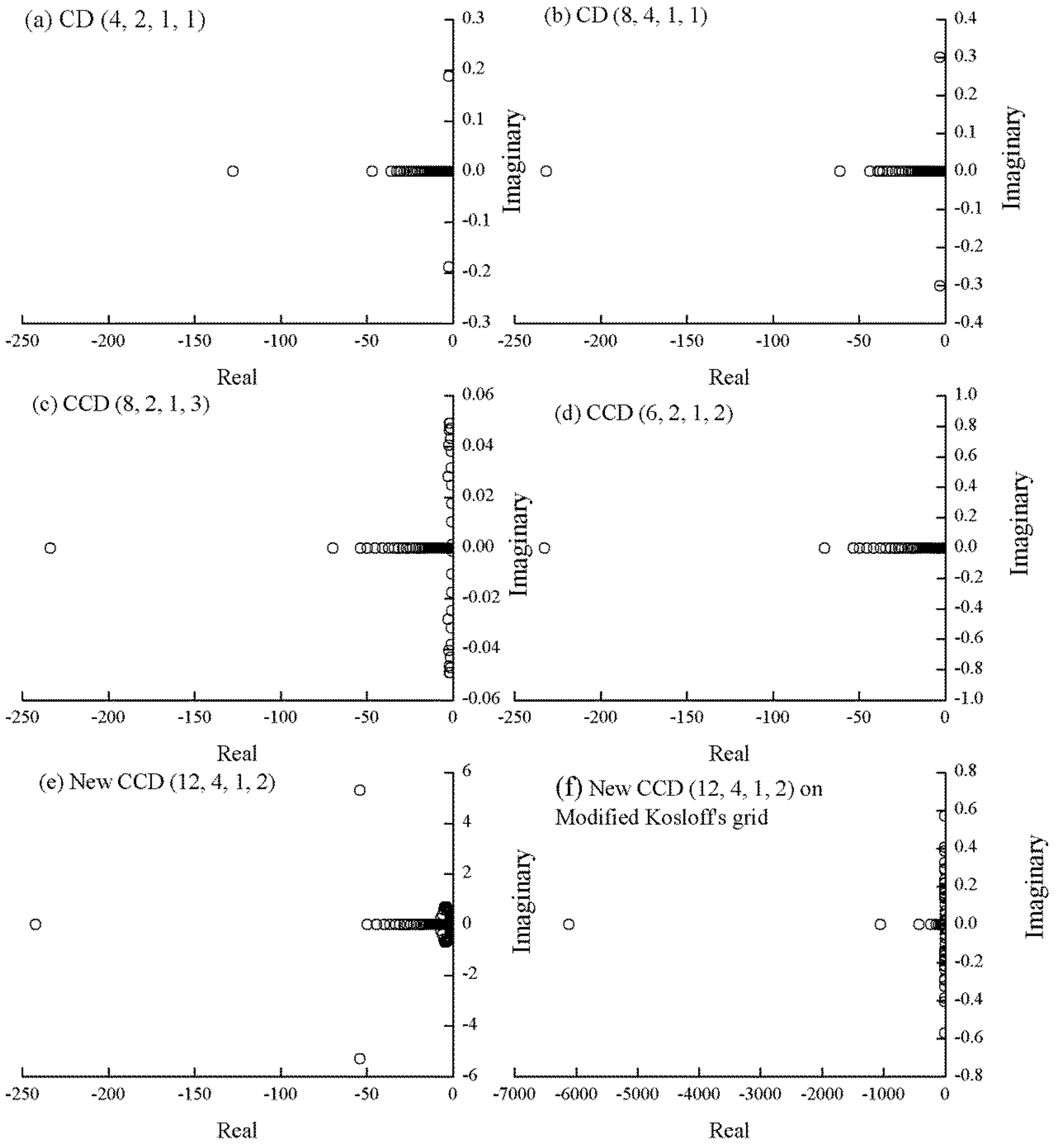

Figure 4. Eigenvalue spectrum for convection-diffusion operator showing the real and imaginary parts of the eigenvalues for the CD and CCD schemes constructed using the grid generation method of Equation (17): (a) CD (4, 2, 1, 1), (b) CD (8, 4, 1, 1), (c) CCD (8, 2, 1, 3), (d) CD (6, 2, 1, 2), (e) New CCD (12, 4, 1, 2). (f) is for new CCD (12, 4, 1, 2) constructed by Modified Kosloff's method (2) in Equation (18).

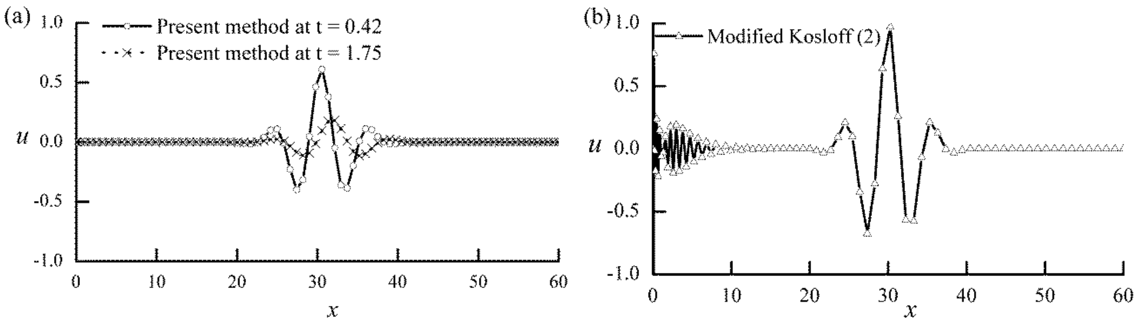

Figure 5. Numerical solutions of the convection-diffusion equation. (a) Present method at *t* = 0.42 and *t* = 1.75 with Δ*t* = 0.035. (b) Modified Kosloff's method (2) at *t* = 0.078 with Δ*t* = 0.0015.

5. Accuracy analysis

Spectral analysis of schemes

The spectral resolution of the finite difference schemes on non-uniform grid can be analyzed by the modified wave number analysis method. Assuming that k denotes the physical wave number, k will be modified to k' and k''^2 due to the errors introduced from finite difference discretizations of the first and second derivatives respectively. The dispersion errors are thus $\mathrm{Re}(k' - k)$ and $\mathrm{Im}(k''^2 - k^2)$, while the dissipation errors are $\mathrm{Im}(k' - k)$ and $\mathrm{Re}(k''^2 - k^2)$. Denoting x_j as the grid point where the finite difference schemes are constructed on, x_i $(i \in I_m, I_n)$ are the grid points, and $\Delta x_i = (x_i - x_j)$, applying the interior scheme on a periodic domain, the substitution of $f(x_i) = \exp(Ikx_i)$ into Equations (15) gives the finite difference scheme in Fourier space. Using the schemes with D = 2 again as an example, the two transformed equations involving k, k' and k''^2 are:

$$\begin{aligned} Ik' = Ik' \sum_{i \in I_n} \rho_{1,i}^{(1)} \exp(Ik\Delta x_i) - k''^2 \sum_{i \in I_n} \rho_{2,i}^{(1)} \exp(Ik\Delta x_i) \\ + \sum_{i \in I_n} \rho_{0,i}^{(1)} \exp(Ik\Delta x_i) + \sum_{i \in I_m} r_i^{(1)} \exp(Ik\Delta x_i) \end{aligned} \tag{31}$$

$$-k''^2 = Ik' \sum_{i \in I_n} \rho_{1,i}^{(2)} \exp(Ik\Delta x_i) - k''^2 \sum_{i \in I_n} \rho_{2,i}^{(2)} \exp(Ik\Delta x_i) \tag{32}$$

$$+\sum_{i\in I_n}\rho_{0,i}^{(2)}\exp(Ik\Delta x_i)+\sum_{i\in I_m}r_i^{(2)}\exp(Ik\Delta x_i)$$

Since the finite difference schemes are constructed on a non-uniform grid, dispersion and dissipation errors will be different at each grid point. Therefore, the maximum dispersion and dissipation errors with the present grid distribution used are plotted below in Figure 6 and Figure 7 wherein the wave number and modified wave number are scaled by $\Delta x_{\max}$, the largest grid size for the finite difference scheme involved, i.e. $w = k\Delta x_{\max}$, $w_1 = k'\Delta x_{\max}$ and $w_2^2 = k''\Delta x_{\max}$.

The present grid generation method in Equation (17) with α_g = 0.975, c = 20, x_c = x_n/4 is used in the spectral analysis for demonstration. Figure 6 and Figure 7 plot the real and imaginary parts of w_1, w_2^2 against w of the new 5-point CCD scheme (12, 4, 1, 2) and the other classical schemes CD (4, 2, 1, 1), CD (8, 4, 1, 1), CD (6, 2, 1, 2), and CCD (8, 2, 1, 3). These plots show that the spectral resolution generally increases with the order of finite difference scheme. For the same stencil, the scheme resolution increases as more high order derivatives are involved and hence the polynomial order increases. For example, in Figure 6 (a), CCD scheme (6, 2, 1, 2) has higher resolution than CD scheme (4, 2, 1, 1) with both 3-point stencil. The new CCD scheme (12, 4, 1, 2) is better than CD scheme (8, 4, 1, 1). Therefore, CCD schemes are generally better than CD schemes with the same stencil. In particular, the new CCD scheme (12, 4, 1, 2) shows negligible dispersion errors up to w = 2.5. Figure 6 (b) shows that all the schemes show negative dissipation error, which is different from the centered schemes on uniform grid. This property helps to stabilize the numerical solution and is consistent with the stability analysis in Section 4. In Figure 7 (a), it can be seen that CD schemes underestimate physical dissipation at high wave number region while CCD schemes tend to overestimate physical dissipation. The additional dissipation from CCD schemes also helps to make the numerical solution stable. Lastly in Figure 7 (b), unlike the case on uniform grid in which dispersion errors are zero, all the schemes have significant dispersion errors at the high wavenumber region, but the one given by the new 5-point CCD scheme (12, 4, 1, 2) is relatively small. By the above comparisons, one can conclude that the new CCD scheme (12, 4, 1, 2) gives the best spectral resolution on the non-uniform grid. It has relatively small dispersion and dissipation errors with scaled wave number up to w = 2.5.

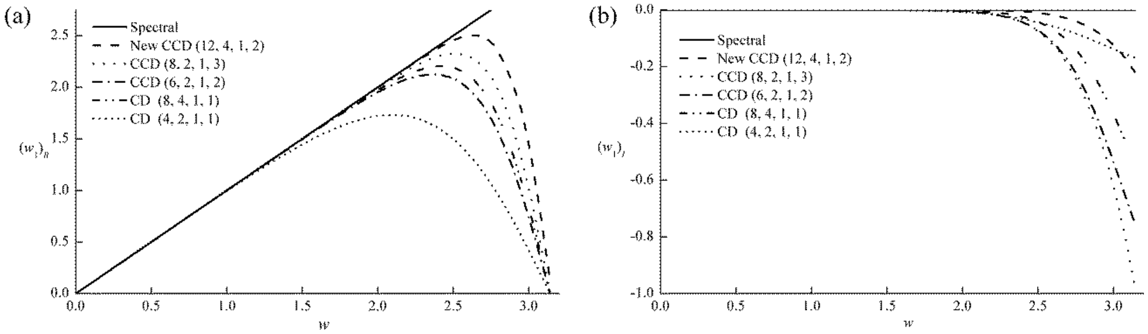

Figure 6. Modified scaled wave number w_1 plotted against scaled wave number w for the finite difference schemes on a non-uniform grid. (a) Real part, (b) Imaginary part.

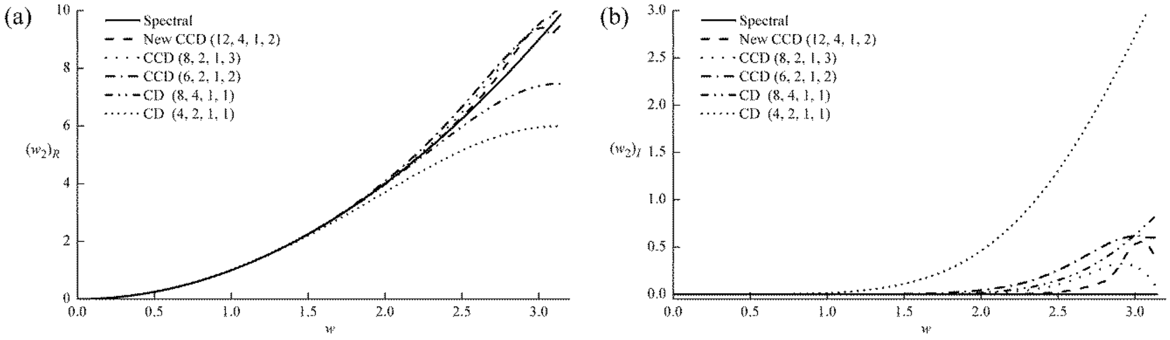

Figure 7. Modified scaled wave number w_2^2 plotted against scaled wave number w for the finite difference schemes on a non-uniform grid. (a) Real part, (b) Imaginary part.

Numerical error analysis of schemes

In order to investigate the accuracy order of different schemes in Table 2 and Table 3, Equation (26) is differentiated with periodic boundary condition, with k = 14. The following grid distribution is used, which is a symmetric version of Equation (17 a) for periodic boundary condition.

$$x_i = \left(1 + \frac{\operatorname{asin}\left(-\alpha_g \cos\left(\frac{\pi i}{n}\right)\right)}{2\operatorname{asin}\left(\alpha_g\right)}\right) \tag{33}$$

where α_g = 0.975.

The L_2 norms of errors $\sqrt{\sum_i^N (u_i - u_{\text{exact}})^2/n}$ are given against the grid number in Table 7 and Table 8 for the first and second derivative respectively. The results show that each scheme demonstrates corresponding order of accuracy close to the expected theoretical values in the mathematical derivations in Section 2.

	CD (4,2,1,1)		CD (8,4,1,1)		CCD (6,2,1,2)		CCD (12,4,1,2)		CCD (8,2,1,3)	
Grid	Error	Order	Error	Order	Error	Order	Error	Order	Error	Order
40	9.61E+00	-	2.38E+00	-	3.38E+00	-	2.82E-01	-	1.25E+00	-
80	2.77E-01	5.1	1.56E-03	10.6	7.58E-03	8.8	1.07E-06	18.0	2.23E-04	12.5
120	4.15E-02	4.7	3.43E-05	9.4	3.85E-04	7.3	2.43E-09	15.0	3.62E-06	10.2
160	1.15E-02	4.5	2.61E-06	9.0	5.38E-05	6.8	4.44E-11	13.9	2.47E-07	9.3
200	4.36E-03	4.3	3.73E-07	8.7	1.23E-05	6.6	2.25E-12	13.4	3.37E-08	8.9
240	2.00E-03	4.3	7.79E-08	8.6	3.78E-06	6.5	2.08E-13	13.1	6.86E-09	8.7

Table 7. Accuracy of different schemes for the first derivative on non-uniform grid.

	CD (4,2,1,1)		CD (8,4,1,1)		CCD (6,2,1,2)		CCD (12,4,1,2)		CCD (8,2,1,3)	
Grid	Error	Order	Error	Order	Error	Order	Error	Order	Error	Order
40	2.89E+02	-	6.02E+01	-	9.83E+01	-	9.68E+00	-	4.37E+01	-
80	1.22E+01	4.6	6.96E-02	9.8	8.35E-01	6.9	2.13E-04	15.5	4.06E-02	9.4
120	1.93E+00	4.6	1.60E-03	9.3	5.09E-02	6.9	6.84E-07	14.2	8.99E-04	8.9
160	5.43E-01	4.4	1.24E-04	8.9	7.52E-03	6.6	1.42E-08	13.5	6.83E-05	8.7
200	2.08E-01	4.3	4.01E-05	5.1	1.76E-03	6.5	7.61E-10	13.1	9.76E-06	8.56
240	9.56E-02	4.3	9.01E-06	8.2	5.49E-04	6.4	7.26E-11	12.9	2.04E-06	10.0

Table 8. Accuracy of different schemes for the second derivative on non-uniform grid.

To demonstrate the computational efficiency of the schemes, Equation (24) is solved with periodic boundary condition on non-uniform grid given in Equation (33). Equation (26) is used as initial condition with k = 14. A 4th order Runge-Kutta scheme is used for temporal integration. The time step is as small as 10^{-5} so that temporal discretization error is small enough compared with spatial discretization error from the present schemes. Equation (24) is integrated for about 6 periods. The discretized linear system is solved with a modified algorithm of Gauss-elimination for band matrix with special consideration of the periodic boundary condition without parallelization. The band matrix is factorized once and only one back substitution process is performed on each Runge-Kutta substep.

Figure 8 (a) and (b) show the error of each scheme on non-uniform grid against number of grid points and computational time (on Intel core i7-2630QM CPU) respectively. Figure 8 (a) clearly shows that as the scheme order increases, the number of grid points required to achieve the same level of accuracy reduces. Comparison between CD (8, 4, 1, 1) and CCD (8, 2, 1, 3) shows that for the same order of accuracy, involving high order derivative can reduce the number of grid points. To achieve the same L_2 norm of error, the new CCD (12, 4, 1, 2) scheme requires least grid points. Figure 8 (b) shows that the efficiency of the scheme depends on the error required. Generally, the tridiagonal schemes CD (4, 2, 1, 1), CCD (6, 2, 1, 2), and CCD (8, 2, 1, 3) are less efficient than those pentadiagonal schemes CCD (8, 4, 1, 1) and new CCD (12, 4, 1, 2). The CCD (8, 2, 1, 3) scheme is inefficient compared with other schemes at every level of error norms. If L_2 norm of error larger than 10^{-8} is satisfactory, CD (8, 4, 1, 1) is the most efficient scheme. However, to achieve a smaller L_2 norm error than 10^{-8}, the new CCD (12, 4, 1, 2) takes less computational time than the CD (8, 4, 1, 1) scheme. In addition, it should be noted that another advantage of CCD scheme type is that they solve high order derivative and the first order derivative simultaneously. This may give CCD type schemes additional performance than CD schemes in certain applications.

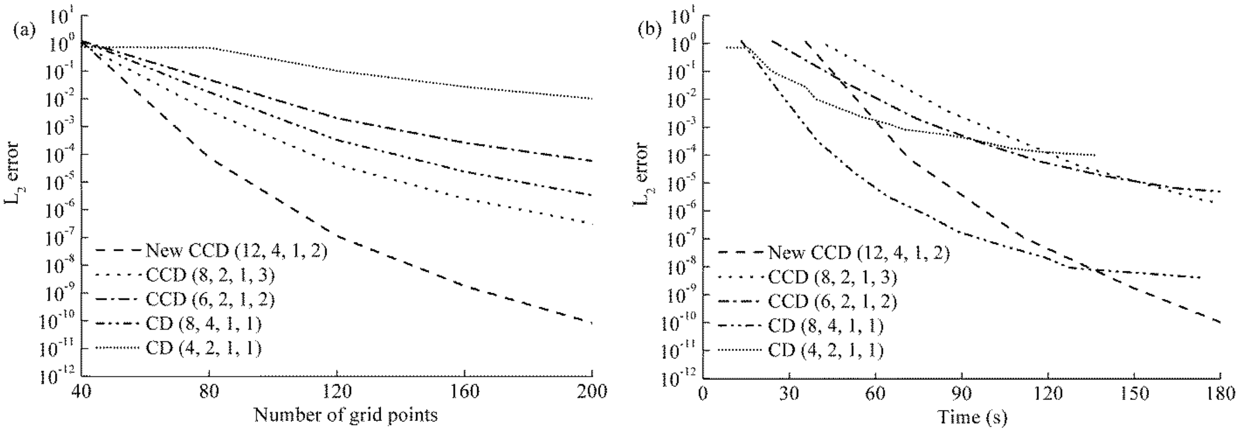

Figure 8. Error of different schemes for solving one-dimensional convection equation on non-uniform grid: (a) error versus number of grid points. (b) error versus computational time.

6. Numerical solution of NS equations

In this section, the advantages of using the high-order CCD scheme (12, 4, 1, 2) on non-uniform grid of Equation (17) are first validated by simulating the classical subharmonic resonance experiment of Kachanov *et al.* [27] wherein the CCD scheme and non-uniform grid are applied to the wall-normal direction. The present simulation methods use significantly less grid points compared with simulation of [16] as will be shown below. To further demonstrate that the present methods are applicable to practical problems, the subharmonic resonance experiment of Borodulin *et al.* [28] in a transitional boundary layer flow with Adverse Pressure Gradient (APG) is simulated and qualitative features of the transition which takes place a short downstream distance are presented.

The physical system targeted for simulation is a boundary layer flow over a flat plate which is disturbed by a blowing and suction strip at a certain upstream location. The rectangular computational domain is shown schematically in Figure 9.

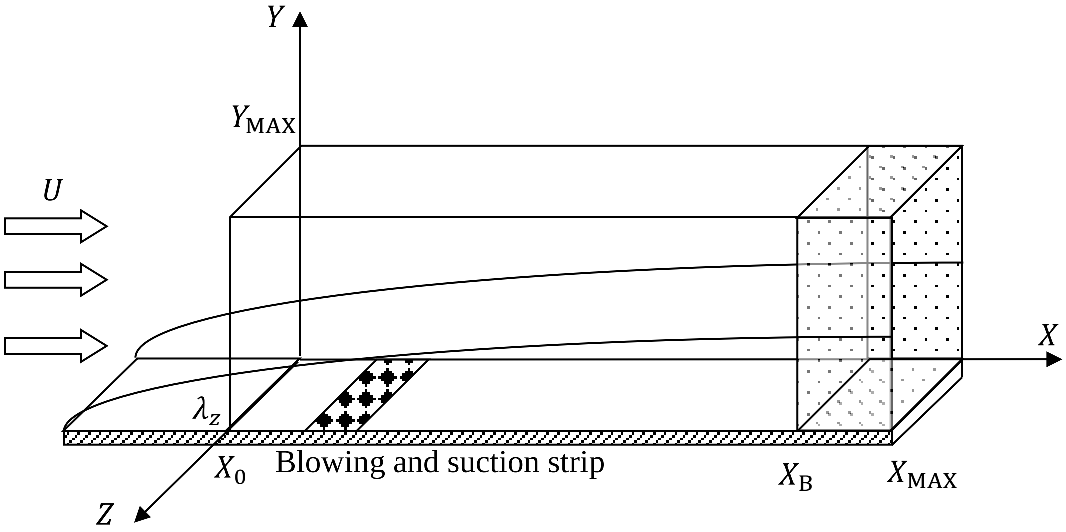

Figure 9. Three-dimensional computational domain. The dotted space indicates a buffer domain. X axis indicates streamwise direction, Y axis the wall-normal direction and Z axis spanwise direction.

Problem formulation

The governing equations and boundary conditions follow that used in [16] to which the reader is referred for further details. The governing equations are the full three-dimensional incompressible Navier-Stokes equations in velocity-vorticity formulation and in non-dimensional form given by.

$$\begin{gathered}\frac{\partial \boldsymbol{\omega}}{\partial t} + (\mathbf{u}\cdot\nabla)\boldsymbol{\omega} = (\boldsymbol{\omega}\cdot\nabla)\mathbf{u} + \nabla^2\boldsymbol{\omega} \\ \nabla^2\mathbf{u} = \nabla\boldsymbol{\omega}\end{gathered} \tag{34}$$

The total flow velocity field $\mathbf{u}(u, v, w)$ and vorticity field $\boldsymbol{\omega}(\omega_x, \omega_y, \omega_z)$ are decomposed into a steady two-dimensional base flow $\mathbf{u_B}(u_B, v_B, w_B)$, $\boldsymbol{\omega}_\mathbf{B}(0,0,\omega_{z_B})$ and an unsteady three-dimensional disturbance flow $\mathbf{u}'(u', v', w')$ and $\boldsymbol{\omega}'(\omega'_x, \omega'_y, \omega'_z)$. The base flow field is first solved and used as the initial condition for the unsteady flow. At the inflow boundary, all the disturbances and their first and second derivatives vanish. No-slip boundary condition is used for the velocities at the wall boundary and wall vorticities are calculated from the velocities. Disturbance velocities decay exponentially and vorticities vanish at the freestream boundary. A buffer is used at the outflow boundary to smoothly damp the disturbance vorticities. Lastly periodic boundary condition is implemented in the spanwise direction.

A Fourier spectral method is used in the spanwise direction. In the streamwise direction, CCD schemes up to 12th-order accuracy as developed in [24] are used on a uniform grid. Upwind CCD scheme co-optimized with 4th order 5-6 alternating stages Runge-Kutta (RK) scheme is used for the streamwise advection terms $\frac{\partial}{\partial x}$. The streamwise diffusion terms $\frac{\partial^2}{\partial x^2}$ are discretized with centered CCD scheme. The grid generation of on Equation (17) is used in wall-normal direction to obtain fine resolution in the near-wall region and grid stretching at the free stream. The new 5-point CCD scheme (12, 4, 1, 2) presented in Table 3 is use for wall norm terms $\frac{\partial}{\partial y}$ and $\frac{\partial^2}{\partial y^2}$. The 2nd-order 5-6 alternating stages SSP-RK scheme given in Appendix A is used for the wall-normal diffusion term $\frac{\partial^2}{\partial y^2}$ to allow larger time step. The details of problem formulations and numerical methods are outlined in the Appendix B with full details given in [26].

Subharmonic resonance in zero pressure gradient (ZPG) boundary layer

This section demonstrates the efficiency of the new CCD scheme on non-uniform grid by simulating the subharmonic resonance experiment of Kachanov *et al.* [27] with ZPG boundary layer. The physical parameters and non-dimensional system follow the ones used in [16]. The computational domain extends from x = 1.427 to 6.827 in the streamwise direction, and from y = 0 to 20.55 in the wall-normal direction (non-uniform grid of Equation (18) (refer to Table 9 for detailed grid information). The spanwise domain covers one subharmonic wave length up to z = 0.2. The disturbance is introduced by the blowing and suction strip mounted over $1.687 \leq x \leq 1.987$. The two- and three- dimensional disturbance waves are denoted as modes (m, k), where m is the multiples of fundamental wave frequency, and k is the multiples of the spanwise wave number. Here (1, 0) is used to denote the TS wave with non-dimensional angular frequency 12.4 and (1/2, 1) is the subharmonic wave. Two grids (coarse and fine) are used here for demonstrating grid independence as listed in Table 9 below where comparison, the parameters used in [16] are also given.

The number of spanwise modes used are the same as in [16]. In the wall-normal direction, most of the grid points are used to cover the wall region with large velocity gradient. Thus only 34 grid points, i.e. 56% of the number in [16] are used in the wall-normal direction for the coarse grid case and 87% for the fine grid. The use of CCD schemes as given earlier in [24] allows the number of grid points in the streamwise direction to be reduced significantly as seen by the Δx interval per TS wave length used. The strong stability and high-order accuracy as demonstrated in Section 4 and 5 also allow a much larger time step when combined with the new CCD schemes in the wall-normal direction applied on the non uniform grid of Equation (18). This enables a direct reduction of the numerical effort when compared to the grid used in [16].

	Wall-normal grid points	$\Delta y_{\max}$	Δx	Δx intervals per TS wave length	Spanwise modes	Δt	Δt interval per TS wave period
Coarse grid	34	1.29	0.03	6.4	2	0.02	25
Fine grid	52	0.77	0.02	9.6	2	0.015	34
Fasel (1990)	60	0.3425	0.00462	41.8	2	0.008	60

Table 9. Grid points (coarse and fine grid) used in the present ZPG boundary layer simulations and in [16].

Figure 10 shows the spatial development of the streamwise disturbance velocity u'. As in the experiments of Kachanov *et al.* (1984), the plotted growth curves are taken from the maximum over the wall-normal direction. The initial amplitude of mode (1, 0) and mode (1/2, 1) are calibrated to match the experiment at $x = 2.2$. The amplification curves generally agree with the experimental results of [27]. The curves start to deviate from the experimental results when $x > 3.4$ with larger amplification rate in the simulation. The mode (1/2, 1) especially shows much stronger amplification at $x > 3.9$.

However, the amplification curves are in good agreement with the simulation results reported in [16].

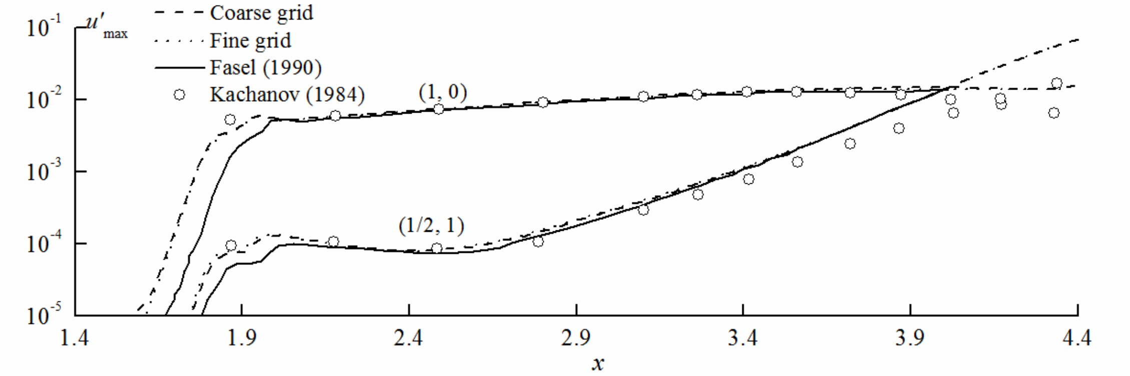

Figure 10. Comparison of amplification curves with the experimental results of Kachanov et al. (1984) and simulations by [16]. The vertical axis is the maximal amplitude of streamwise disturbance u' along the wall-normal direction.

The amplitude distribution in the wall-normal direction at $x = 3.7$ is shown in Figure 11. The agreement for mode (1, 0) between the simulation and experiments is generally good, but the simulation shows a slightly smaller amplitude. Consistent with the amplification in Figure 10, mode (1/2, 1) has a larger amplitude than that in the experiments.

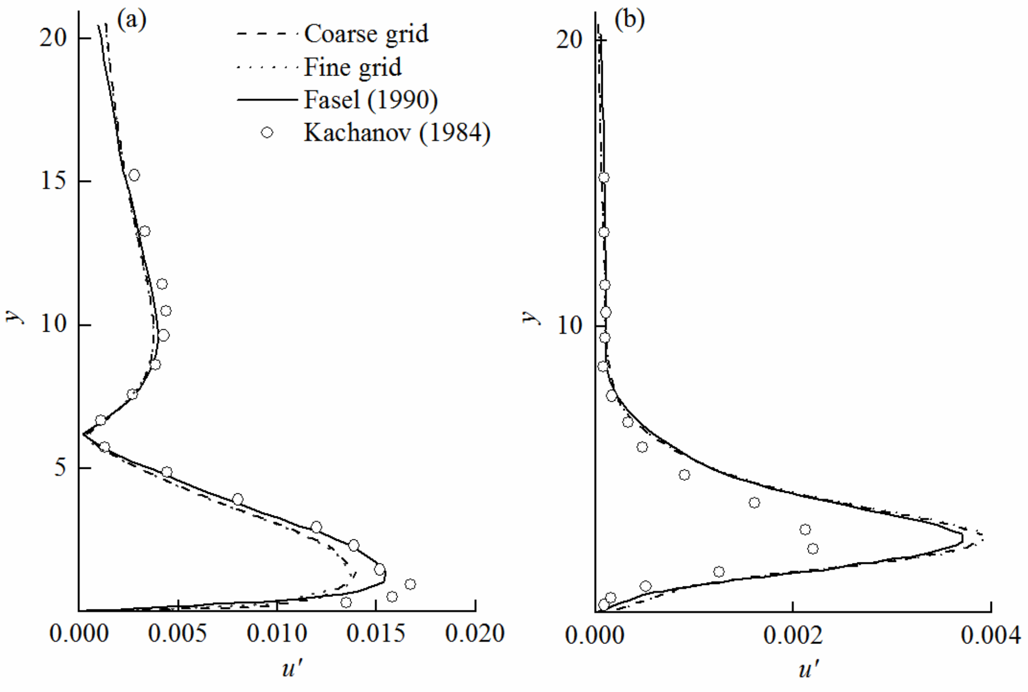

Figure 11. Wall-normal amplitude distributions of the streamwise disturbance velocities u' at x = 3.7 normalized by freestream velocity and comparisons with the experimental results of [27] and simulation results by [16], (a) mode (1, 0), (b) mode (1/2, 1).

Simulation of subharmonic resonance in adverse pressure gradient (APG) boundary layer

The numerical model is further validated by the simulation of subharmonic resonance in APG boundary layer transition flow with Hartree parameter of -0.115, based on the experiments by Borodulin *et al.* [28]. Simulations are performed in two cases with different grid sizes. Case 1 (coarse grid) focuses on the weakly non-linear stage, so that a relatively coarse grid can be used. Case 2 (fine grid) covers a larger downstream region and higher Reynolds number, where vortex evolution takes places near the wall region necessitating finer grid sizes. In the later comparisons, X, Y and Z denote the dimensional coordinates in the streamwise, wall-normal, and spanwise directions while T and u' denote the dimensional time and streamwise disturbance velocity, respectively. The initial disturbance strength of TS and subharmonic waves are calibrated to match the experiments at X = 350 mm, where the initial amplitudes of the fundamental and subharmonic waves are 0.1% and 0.01% of the freestream velocity, respectively. The disturbance frequency of TS wave is 109.1 Hz with subharmonic frequency 54.55 Hz. The grid sizes are listed in Table 10 below.

	Wall-normal grid points	$\Delta y_{\max}$	Δx	Δx interval per TS wave length	Spanwise modes	Δt	Δt interval per TS wave period
Coarse grid	60	0.56 mm	0.2 mm	15.2	4	3.2×10^{-5} s	280
Fine grid	80	0.45 mm	0.08 mm	38	16	1.3×10^{-5} s	700

Table 10 Grid points used in the present APG boundary layer simulations.

Figure 12 shows the spatial development of the wave components for the streamwise disturbance velocity u'. As in the experiments, the growth curves are taken from the maximum in the wall-normal direction. The main trend follows the experiment: mode (1, 0) grows steadily, but mode (1/2, 1) amplifies dramatically and its amplitude exceeds that of mode (1, 0). Although the amplification of the subharmonic mode is slightly weaker in the present simulation, the agreement with the experimental results is generally remarkable.

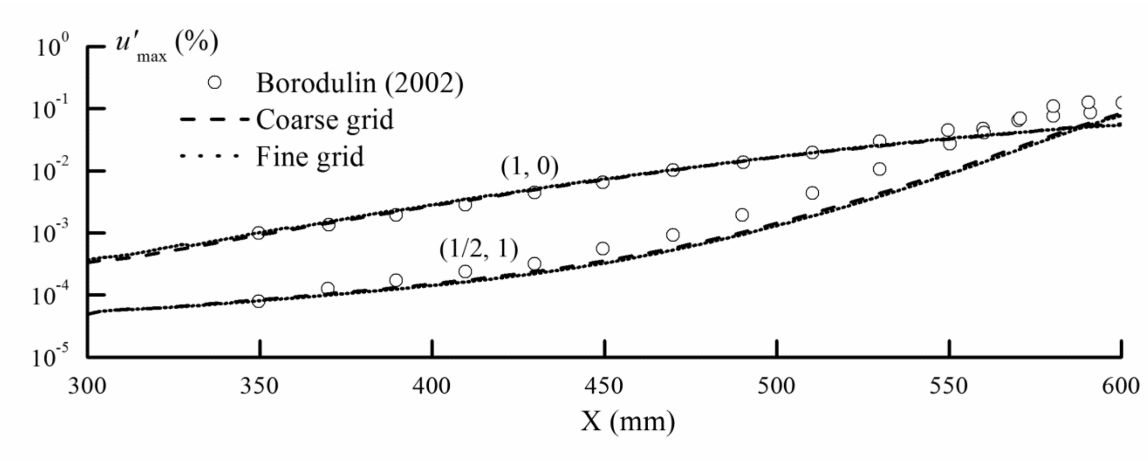

Figure 12. Amplification curves of fundamental and subharmonic waves compared with experimental results in [28]. The vertical axis is the maximum streamwise disturbance velocity u' normalized by the freestream velocity.

Figure 13 show a comparison between the amplitude profiles of u', specifically the amplitude of mode (1, 0) against the wall-normal distance normalized by the boundary layer displacement thickness δ_1. Although the amplitude in the present simulation is slightly larger, the distribution generally agrees with the experimental results. The amplitude of mode (1/2, 1) has further been normalized by its maximum for the comparison with the results reported in [28].

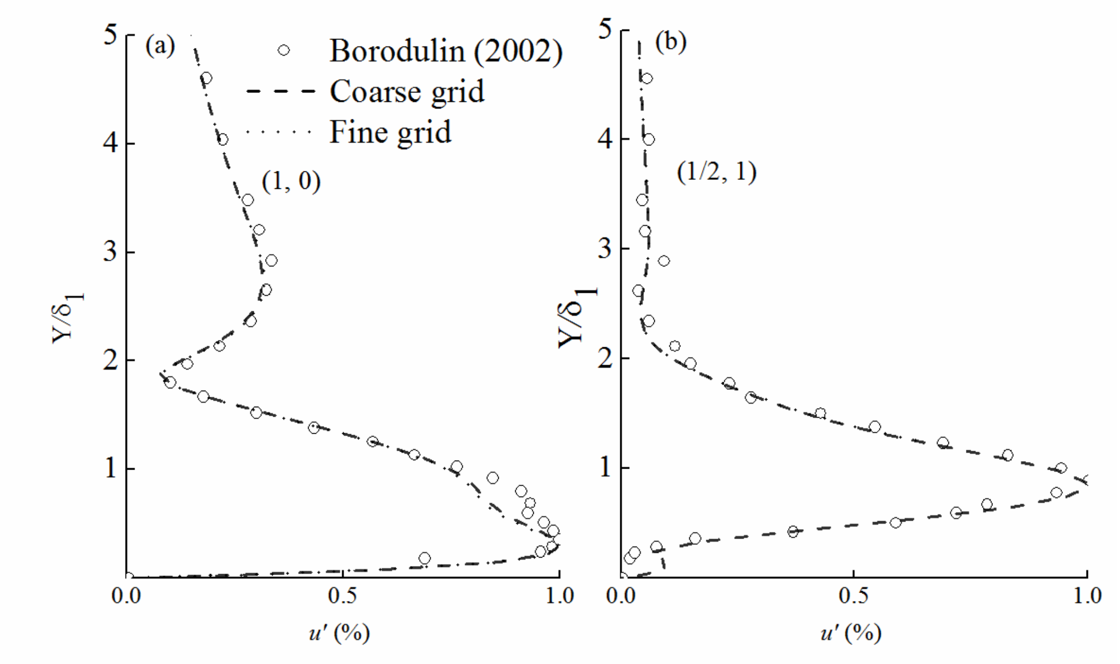

Figure 13. Amplitude distributions of streamwise disturbance velocity *u'* at X = 450 mm compared with experimental results in [28]. The horizontal axis is the wall-normal coordinate Y normalized by the boundary layer displacement thickness δ_1; (a) fundamental TS wave, *u'* normalized by freestream velocity, (b) subharmonic wave reproduced from [28], *u'* normalized by its local maximum.

The above quantitative comparisons show good agreement with experiments at the weakly non-linear stage of transition even when using a coarse grid (Case 1). The finer resolution (Case 2) does not further improve. While experimental measurements at locations further downstream disturbance are not available for comparison, the simulated vortex evolution using a fine grid (Case 2) will be shown to demonstrate the subsequent stable numerical behavior and that the expected evolution as described in [10, 12] is obtained.

Figure 14 shows the streamwise disturbance contour u' at T = 0.1075 s at different Y values. For Y = 3.4 mm (Figure 14 (a)), there are five three-dimensional structures arranged in a staggered pattern along the streamwise direction. A structure is first seen at around X = 0.53 m with a weak negative u' amplitude. These structures show increasingly negative amplitudes for locations further downstream. At the same time, they gradually evolve from a rhombus-shape (X = 0.56 m) to the typical Λ-shape (X = 0.63 m). At X = 0.67 m, the Λ-structure further stretches and a low speed streak forms at its tip. Figure 14 (b) shows the streamwise disturbance contour u' at a location Y = 7.1

mm, further away from the wall. Here, the Λ-structures are weaker, however, there are strong velocity reduction at the tips of the Λ-structures, especially at X = 0.68 m. The locations of negative velocity are associated with the formation of the first ring-like vortices as discussed below.

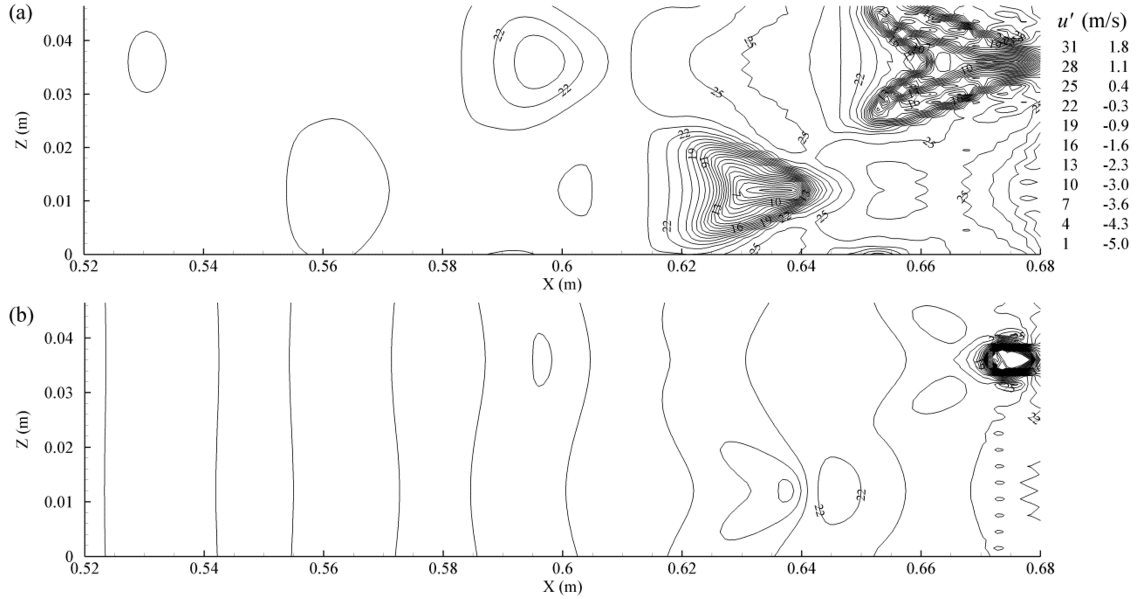

Figure 14. Streamwise disturbance velocity contour *u'* (m/s) at T = 0.1075 s. The vertical axis is the spanwise coordinate and the horizontal axis is the streamwise coordinate, (a) Y = 3.4 mm, (b) Y = 7.1 mm.

Figure 15 plots the streamwise disturbance velocity gradient against the wall-normal direction at the same time T of Figure 14, but viewed at different spanwise locations. The relationship between the high shear layer and the three-dimensional structures can be clearly seen. In both Figure 15 (a) and (b), a high shear layer is first developed at region close to the wall with certain streamwise periodicity from X = 0.52 to X = 0.59 m. After X = 0.6 m, this high shear layer spreads towards the free stream direction and gives the three-dimensional structure. The coherent structure at X = 0.62 to 0.64 m in Figure 15 (a) is the same Λ-structure at that in Figure 14 (a), while the coherent structure at X = 0.6 m in Figure 15 (b) is the same rhombus-shape structure in Figure 14 (a). The numerical results show the development of the three-dimensional coherent structures in boundary layer transition along with the corresponding formation of a high shear layer as successfully captured by the present non-linear grid distribution and the new 5-point CCD scheme.

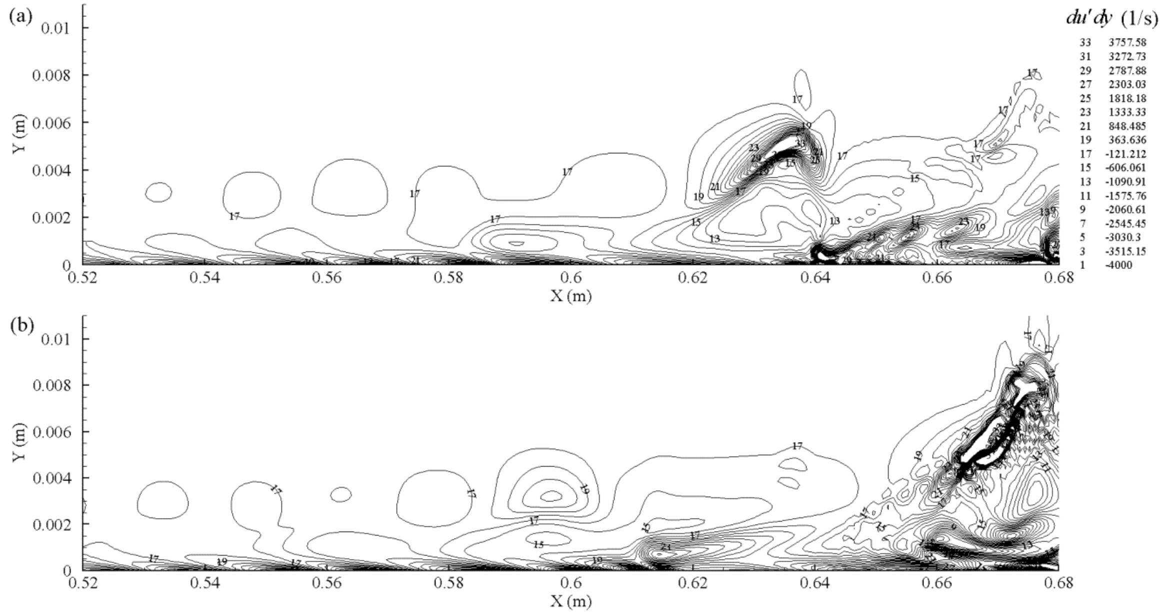

Figure 15. Streamwise disturbance velocity gradient contour *du/dy* (1/s) at T = 0.1075 s. The vertical axis is the spanwise coordinate and the horizontal axis is the streamwise coordinate, (a) Z = 10.5 mm, (b) Z = 37.5 mm.

A vortex can be visualized by using the Q-criterion developed in [29]. Figure 16 shows three vortex groups in different evolution stage of subharmonic resonance. The vortices are aligned in a staggered-pattern in the downstream direction. At X = 0.61 m, a primary Λ-vortex forms. At X = 0.64 m, a typical Ω-vortex can be observed and the 1st and 2nd ring-like vortices are generated near the tip of the main vortex. At X = 0.67 m, the two legs of the vortex starts to break down and a more mature shape of the first ring-like vortex can be observed. Figure 16 shows that the present simulation results capture the main features of vortical structures in subharmonic resonance, as summarized in [10, 12].

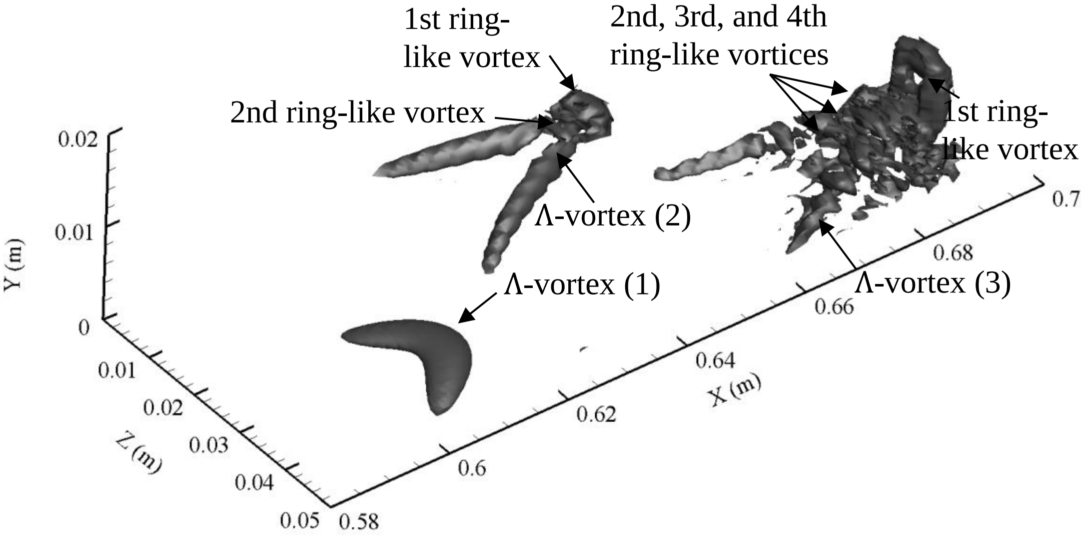

Figure 16. Visualization of vortex evolution by use of the Q-criterion at T = 0.1101 s.

7. Conclusion

In this study, an interpolation based method is developed to derive high-order finite difference schemes over non-uniform grids. The schemes are first constructed by interpolation methods, which can involve arbitrary order of derivatives and grid points. It is further shown that via linear operation, more finite difference schemes can be constructed that involves specific derivative and/or function values at certain grid point. Via this general method, various classical schemes can be constructed, including the 3-point CD, CCD, and SCD schemes.

A new 5-point CCD scheme is developed together with a new non-uniform grid generation function for grid clustering near wall region and grid stretching away. Most of the CD and CCD schemes constructed on this new grid are numerically stable and demonstrate high spectral resolution. It further offers improvement over finite element methods which only provide a weak form solution of the mass conservation law [34, 35], since the present scheme can satisfy mass conservation locally. It is also capable of arbitrarily high order accuracy compared to both finite element and high order finite volume methods where the accuracy is lower, typically 4th order or less [34, 36].

The new 5-point CCD scheme has been demonstrated via numerical solutions of the full incompressible NS equations for simulation of subharmonic resonance in ZPG and APG boundary layers. The simulation results in the weakly non-linear stage are in general agreement with the experiments. Specifically in simulation of Kachanov *et al.*’s experiments [27], the present numerical method require much less grid points than the simulations of [16]. In the simulation of Borodulin *et al.*'s experiment [28], the present results show the vortex evolution process in subharmonic resonance. These calculations demonstrate that the developed general method for deriving high-order finite difference schemes and grid generation are applicable to simulations of boundary layer transitions.

References

[1] Lele SK. Compact Finite Difference Schemes with Spectral-Like Resolution. J Comput Phys. 1992;103:16-42.

[2] Ghader S, Mohebalhojeh AR. On the Spectral Convergence of the Supercompact Finite Difference Schemes for the f-plane Shallow-Water Equations. Monthly Weather Review. 2009.

[3] Chu PC, Fan CW. A Three-Point Combined Compact Difference Scheme. J Comput Phys. 1998;140:370-99.

[4] Chu PC, Fan CW. A Three-Point Sixth-Order Nonuniform Combined Compact Difference Scheme. J Comput Phys. 1999;148:663-74.

[5] Shen MY, Zhang ZB, Niu XL. A New Way for Constructing High Accuracy Shock-Capturing Generalized Compact Difference Schemes. COMPUT METHOD APPL M. 2003;192:2703-25.

[6] Esfahanian V, Ghader S, Ashrafi K. Accuracy Analysis of Super Compact Scheme in Non-Uniform Grid with Application to Parabolized Stability Equations. Int J Numer Methods Fluids. 2004;46:485-505.

[7] Shukla RK, Zhong XL. Derivation of High-Order Compact Finite Difference Schemes for Non-Uniform Grid Using Polynomial Interpolation. J Comput Phys. 2005;204:404-29.

[8] Sengupta TK, Lakshmanan V, Vijay V. A New Combined Stable and Dispersion Relation Preserving Compact Scheme for Non-Periodic Problems. J Comput Phys. 2009;228:3048-71.

[9] Hermanns M, Hernandez JA. Stable High-Order Finite-Difference Methods Based on Non-Uniform Grid Point Distributions. Int J Numer Methods Fluids. 2008;56:233-55.

[10] Herbert T. Secondary Instability of Boundary-Layers. Annu Rev Fluid Mech. 1988;20:487-526.

[11] Kachanov YS. Physical Mechanisms of Laminar-Boundary-Layer Transition. Annu Rev Fluid Mech. 1994;26:411-82.

[12] Bake S, Fernholz HH, Kachanov YS. Resemblance of K- and N-regimes of Boundary-Layer Transition at Late Stages. European Journal of Mechanics B-Fluids. 2000;19:1-22.

[13] Liu Z, Liu C. Fourth Order Finite-Difference and Multigrid methods for Modeling Instabilities in Flat-Plate Boundary Layers-2D and 3D Approaches. Computers & Fluids. 1994;23:955-82.

[14] Davies C, Carpenter PW. A Novel Velocity–Vorticity Formulation of the Navier–Stokes Equations with Applications to Boundary Layer Disturbance Evolution. J Comput Phys. 2001;172:119-65.

[15] Meitz HL, Fasel HF. A Compact-Difference Scheme for the Navier–Stokes Equations in Vorticity–Velocity Formulation. J Comput Phys. 2000;157:371-403.

[16] Fasel H. Numerical Investigation of the Three-Dimensional Development in Boundary-Layer Transition. Aiaa J. 1990 b;28:29-37.

[17] Zhong XL, Tatineni M. High-order Non-uniform Grid Schemes for Numerical Simulation of Hypersonic Boundary-layer Stability and Transition. J Comput Phys. 2003;190:419-58.

[18] Nihei T, Ishii K. Flow simulation using combined compact difference scheme with spectral-like resolution. In: Fujii K, Nakahashi K, Obayashi S, Komurasaki S, editors. New Developments in Computational Fluid Dynamics. New York: Springer; 2005. p. 206-14.

[19] Shukla RK, Tatineni M, Zhong XL. Very high-order compact finite difference schemes on non-uniform grids for incompressible Navier-Stokes equations. J Comput Phys. 2007;224:1064-94.

[20] Ma Y, Fu. D. Super compact finite difference method (SCFDM) with arbitrarily high accuracy. Computational Fluid Dynamics Journal. 1996;5:259-76.

[21] Kosloff D, Talezer H. A Modified Chebyshev Pseuduo-Spectral Method with an O(N-1) Time Step Restriction. J Comput Phys. 1993;104:457-69.

[22] Anderson JD. Computational fluid dynamics:The basics with applications: McGraw-Hill; 1995.

[23] Hirsch C. Numerical Computation of Internal and External Flows: Fundamentals of Computational Fluid Dynamics. second ed. Amsterdam; London: Butterworth-Heinemann; 2007.

[24] Chen WJ, Chen JC. Combined compact difference method for solving the incompressible Navier-Stokes equations. Int J Numer Methods Fluids. 2012;68:1234-56.

[25] Gottlieb S. On High Order Strong Stability Preserving Runge-Kutta and Multi Step Time Discretizations. J Sci Comput. 2005;25:105-28.

[26] Chen W. Numerical Simulation of Boundary Layer Transition by Combined Compact Difference Method: Nanyang Technological University; 2013.

[27] Kachanov YS, Levchenko VY. The Resonant Interaction of Disturbances at Laminar Turbulent Transition in a Boundary-Layer. J Fluid Mech. 1984;138:209-47.

[28] Borodulin VI, Kachanov YS, Koptsev DB. Experimental Study of Resonant Interactions of Instability Waves in a Self-Similar Boundary Layer with an Adverse Pressure Gradient: I. Tuned Resonances. J Turbul. 2002 b;3.

[29] Hunt JCR, Wray AA, Moin P. Eddies, stream, and convergence zones in turbulent flows. Center for Turbulent Research Report CTR-S81988. p. 193.

[30] Hu FQ, Hussaini MY, Manthey JL. Low-dissipation and Low-dispersion Runge-Kutta Schemes for Computational Acoustics. J Comput Phys. 1996;124:177-91.

[31] Ruuth SJ, Spiteri RJ. High-order Strong-Stability-Preserving Runge-Kutta Methods with Downwind-Biased Spatial Discretizations. SIAM J Numer Anal. 2004;42:974-96.

[32] Ketcheson DI. Highly Efficient Strong Stability-Preserving Runge-Kutta Methods with Low-Storage Implementations. SIAM J Sci Comput. 2007;30:2113-36.

[33] Peyret, Roger. Spectral methods for incompressible viscous flow: Springer; 2002.

[34] Hymana JM, Knappc RJ, Scovelb JC. High order finite volume approximations of differential operators on nonuniform grids. Physica D: Nonlinear Phenomena. 1992;60:112-38.

[35] Strang G, Fix GJ. An Analysis of the Finite Element Method. 1973.

[36] Wang Z, Yeo KS, Khoo BC. Spatial direct numerical simulation of transitional boundary layer over compliant surfaces. Computers & Fluids. 2005;34:1062-95.

Appendix A Temporal scheme and stability analysis

The general s-stage RK scheme is used to integrate an unknown function u as follows. For i = 1, …, s (s = 5 or 6), compute

$$K_i = \Delta t \mathcal{L}(u^n + r_i K_{i-1}) \tag{A.1}$$

$$u^{n+1} = u^n + K_s \tag{A.2}$$

where $\mathcal{L}$ is the spatial discretization operator as in Equation (22). Amplification factors z_P for temporal stability analysis can be obtained following ([23])

$$z_P = 1 + \sum_{i=1}^{s} \tilde{r}_i \left(\Delta t \tilde{\mathcal{L}}\right)^i \tag{A.3}$$

where $\tilde{\mathcal{L}}$ is the spectral mode of $\mathcal{L}$ and the coefficients $\tilde{r}_i$ are related to the coefficients in Equation (A.1) with the following relationship given in [30]:

$$\begin{gathered} \tilde{r}_2 = r_s, \\ \tilde{r}_3 = r_s r_{s-1}, \\ \vdots \\ \tilde{r}_s = r_s r_{s-1} \dots r_2 \end{gathered} \tag{A.4}$$

Based on the 2nd order Strong Stability Preserving Runge-Kutta (SSP-RK) scheme developed by [31] and its low-storage implementation form given in [32], the coefficients $\tilde{r}_i$ of 5-6 alternating stage SSP-RK scheme (denoted by RK(2,5-6)) are given in Table A.1.

	1	2	3	4	5	6
5-stage $\tilde{r}_i$	1	$\frac{1}{2}$	$\frac{1}{8}$	$\frac{1}{64}$	$\frac{1}{1280}$	-
6-stage $\tilde{r}_i$	1	$\frac{1}{2}$	$\frac{2}{15}$	$\frac{1}{50}$	$\frac{1}{625}$	$\frac{1}{18750}$

Table A.1. Coefficients of RK (2, 5-6) scheme.

Two types of RK method have been used in this paper for different spatial discretizations. The first 2nd order RK (2, 5-6) scheme is used for the 2nd derivative with grid clustering in the wall normal direction and the 4th order RK (4, 5-6) developed in [24], is for other derivatives. The stability "footprint" can be shown to be larger for RK (2, 5-6) than that of RK (4, 5-6) (Chen (2013)) [26] and therefore the RK (2, 5-6) scheme allows a larger temporal step. Δt can be adjusted to make $\Delta t \mathcal{L}_j$ satisfy stability condition, i.e. be bounded by the "footprint" $\mathcal{R}$. Formally Δt is determined by

$$\Delta t \leq \frac{\sup|\mathcal{R}|}{\sup|\mathcal{L}_j|} \tag{A.5}$$

Appendix B Formulation of boundary layer transition simulation

The governing equations in Section 6 are related to their dimensional counterparts, denoted by bars, as follows:

$$\begin{aligned} Re &= \frac{\overline{U}_\infty \overline{L}}{\overline{\nu}}, \qquad x = \frac{\overline{x}}{\overline{L}}, \qquad y = \frac{\overline{y}\sqrt{Re}}{\overline{L}}, \qquad z = \frac{\overline{z}}{\overline{L}}, \\ t &= \frac{\overline{U}_\infty \overline{t}}{\overline{L}}, \qquad u = \frac{\overline{u}}{\overline{U}_\infty}, \qquad v = \frac{\overline{v}\sqrt{Re}}{\overline{U}_\infty}\ , \qquad w = \frac{\overline{w}}{\overline{U}_\infty}. \end{aligned} \tag{B.1}$$

where $\overline{L}$ is the characteristic length, $\overline{U}_\infty$ is the freestream velocity, $\overline{\nu}$ is the kinematic viscosity, and Re is a reference Reynolds number. The NS equations are solved in a vorticity-velocity formulation with vorticity components given as

$$\omega_x = \frac{1}{Re}\frac{\partial v}{\partial z} - \frac{\partial w}{\partial y}, \omega_y = \frac{\partial w}{\partial x} - \frac{\partial u}{\partial z}, \omega_z = \frac{\partial u}{\partial y} - \frac{1}{Re}\frac{\partial v}{\partial x} \tag{B.2}$$

The total flow field $(\boldsymbol{V}, \boldsymbol{\Omega})$ is decomposed into a steady two-dimensional base flow $(\boldsymbol{V_B}, \boldsymbol{\Omega_B})$ and an unsteady three-dimensional disturbance flow $(\boldsymbol{V'}, \boldsymbol{\Omega'})$ written as

$$\boldsymbol{V}(t,x,y,z) = \boldsymbol{V_B}(x,y,z) + \boldsymbol{V}'(t,x,y,z), \tag{B.3}$$

$$\boldsymbol{\Omega}(t,x,y,z) = \boldsymbol{\Omega_B}(x,y,z) + \boldsymbol{\Omega}'(t,x,y,z), \tag{B.4}$$

with

$$\boldsymbol{V_B} = \{u_B, v_B, 0\}, \qquad \boldsymbol{\Omega_B} = \left\{0, 0, \omega_{z_B}\right\} \tag{B.5}$$

$$\boldsymbol{V}' = \{u', v', w'\}, \qquad \boldsymbol{\Omega}' = \left\{\omega'_x, \omega'_y, \omega'_z\right\}. \tag{B.6}$$

In this form the NS equations consist of three vorticity transport equations:

$$\frac{\partial \omega'_x}{\partial t} + \frac{\partial a}{\partial y} - \frac{\partial c}{\partial z} = \frac{1}{Re}\frac{\partial^2 \omega'_x}{\partial x^2} + \frac{\partial^2 \omega'_x}{\partial y^2} + \frac{1}{Re}\frac{\partial^2 \omega'_x}{\partial z^2}, \tag{B.7}$$

$$\frac{\partial \omega'_y}{\partial t} - \frac{\partial a}{\partial x} + \frac{\partial b}{\partial z} = \frac{1}{Re}\frac{\partial^2 \omega'_y}{\partial x^2} + \frac{\partial^2 \omega'_y}{\partial y^2} + \frac{1}{Re}\frac{\partial^2 \omega'_y}{\partial z^2}, \tag{B.8}$$

$$\frac{\partial \omega'_z}{\partial t} + \frac{\partial c}{\partial x} - \frac{\partial b}{\partial y} = \frac{1}{Re}\frac{\partial^2 \omega'_z}{\partial x^2} + \frac{\partial^2 \omega'_z}{\partial y^2} + \frac{1}{Re}\frac{\partial^2 \omega'_z}{\partial z^2}, \tag{B.9}$$

where

$$a = v'\omega'_x - u'\omega'_y + v_B{}'\omega'_x - u_B\omega'_y, \tag{B.10}$$

$$b = w'^{\omega'_y} - v'\omega'_z - v_B\omega'_z - v'\omega_{z_B}, \tag{B.11}$$

$$c = u\omega'_z - w\omega'_x + u_B\omega'_z + u'\omega_{z_B}. \tag{B.12}$$

and three velocity Poisson's equations:

$$\frac{\partial^2 u'}{\partial x^2} + \frac{\partial^2 u'}{\partial z^2} = -\frac{\partial \omega'_y}{\partial z} - \frac{\partial^2 v'}{\partial x \partial y}, \tag{B.13}$$

$$\frac{1}{Re}\frac{\partial^2 v'}{\partial x^2} + \frac{\partial^2 v'}{\partial y^2} + \frac{1}{Re}\frac{\partial^2 v'}{\partial z^2} = \frac{\partial \omega'_x}{\partial z} - \frac{\partial \omega'_z}{\partial x}, \tag{B.14}$$

$$\frac{\partial^2 w'}{\partial x^2} + \frac{\partial^2 w'}{\partial z^2} = \frac{\partial \omega'_y}{\partial x} - \frac{\partial^2 v'}{\partial y \partial z}. \tag{B.15}$$

As periodicity in the spanwise direction z is assumed, the disturbance flow variables $(\boldsymbol{V}', \boldsymbol{\Omega}')$ and the terms (a, b, c) are expanded with Fourier modes

$$(\boldsymbol{V}', \boldsymbol{\Omega}', a, b, c) = \sum_{k=0}^{K-1} (\boldsymbol{V}'_k, \boldsymbol{\Omega}'_k, a_k, b_k, c_k) \exp(Ik\gamma_z) \tag{B.16}$$

where $I = \sqrt{-1}$ and γ_z is the lowest spanwise Fourier mode related to the spanwise wavelength λ_z by

$$\gamma_z = \frac{2\pi}{\lambda_z} \tag{B.17}$$

Substituting Equations (B.16) into Equations (B.7) to (B.15) give K sets of governing equations for each (x, y)-plane integration domain. The nonlinear terms a, b and c of the vorticity transport equations are evaluated pseudo-spectrally using Fast Fourier Transform and with the 3/2 rule applied for de-aliasing (e.g. [33]).

All disturbance variables are specified as zero as inflow boundary conditions. At the freestream boundary, the vorticities vanish and the disturbance v' decay exponentially as

$$\frac{\partial v'}{\partial y} = -\frac{\alpha^*}{\sqrt{Re}} v' \tag{B.18}$$

where $\alpha^* = \sqrt{\alpha_x^2 + \gamma_z^2}$ and α_x is the streamwise wave number. At the wall, no-slip conditions are imposed on the disturbance velocity and the disturbance vorticities are calculated from the equations below:

$$\frac{\partial^2 \omega_x'}{\partial x^2} + \frac{\partial^2 \omega_x'}{\partial z^2} = -\frac{\partial \omega_y'}{\partial x \partial y} + \frac{\partial}{\partial z}\left(\frac{1}{Re}\frac{\partial^2 v'}{\partial x^2} + \frac{\partial^2 v'}{\partial y^2} + \frac{1}{Re}\frac{\partial^2 v'}{\partial z^2}\right), \tag{B.19}$$

$$\omega_y' = 0, \tag{B.20}$$

$$\frac{\partial^2 \omega_z'}{\partial x} = \frac{\partial \omega_x'}{\partial z} - \left(\frac{1}{Re}\frac{\partial^2 v'}{\partial x^2} + \frac{\partial^2 v'}{\partial y^2} + \frac{1}{Re}\frac{\partial^2 v'}{\partial z^2}\right). \tag{B.21}$$

A buffer domain method is used near the outflow boundary region with details in [24].

The disturbance signals in subharmonic resonance consist of two main components: the signal corresponding to the fundamental two-dimensional TS wave and three-dimensional small subharmonic wave. The disturbances are introduced from the wall-normal velocity component $\hat{v}'(x, y, k)$ in the spanwise spectral space. The TS wave is generated by

$$\hat{v}'(x, 0, k) = \mathrm{A}_k f(x) \sin(\beta t) \tag{B.22}$$

where A_k is used to adjust the amplitudes of different spectral modes and β is the disturbance frequency. $f(x)$ is given as

$$f(x) = \begin{cases} 24.96\xi^6 - 56.16\xi^5 + 31.2\xi^4 & \xi = \dfrac{x - x_1}{x_{\mathrm{st}} - x_1} \quad x_1 < x < x_{\mathrm{st}} \\ -24.96\xi^6 + 56.16\xi^5 - 31.2\xi^4 & \xi = \dfrac{x_1 - x}{x_2 - x_{\mathrm{st}}} \quad x_{\mathrm{st}} < x < x_2 \end{cases} \tag{B.23}$$

A_k is adjusted to change the streamwise disturbance velocity u' to match experiments.

The numerical schemes for each term in Equations (B.7) to (B.15) are summarized in table B.2 below. Full details of the above method are found in [26].

$\frac{\partial}{\partial z}, \frac{\partial^2}{\partial z^2}$	Spectral method
$\frac{\partial}{\partial x}$	12th order upwind CCD scheme on uniform grid presented in [24]
$\frac{\partial^2}{\partial x^2}$ all equations except (B.14)	12th order centered CCD scheme on uniform grid presented in [24]
$\frac{\partial^2}{\partial x^2}$ in equation (B.14)	12th order explicit centered scheme presented in [26]
$\frac{\partial}{\partial y}, \frac{\partial^2}{\partial y^2}$	12th order centered CCD scheme on non-uniform grid in present paper
$\frac{\partial}{\partial t}$	RK (4, 5-6) for $\frac{\partial}{\partial z}, \frac{\partial^2}{\partial z^2}, \frac{\partial}{\partial x}, \frac{\partial^2}{\partial x^2}, \frac{\partial}{\partial y}$. RK (2, 5-6) for $\frac{\partial^2}{\partial y^2}$

Table B.1. Summary of schemes applied to each term